



UNIVERSITY OF AMSTERDAM



MSc Physics and Astronomy
Track: Astronomy & Astrophysics

MASTER THESIS

OB supergiants in High-Mass X-ray Binaries

**Revisiting the physical parameters of the OB supergiants in 6 binary
systems hosting an eclipsing X-ray pulsar**

by

**Luuk van Vliet
12251925 (UVA)**

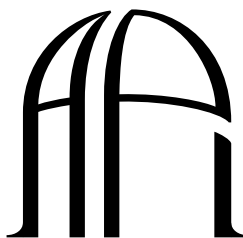
August 22, 2024

60 ECTS

July 2023 - August 2024

Supervisors:
Prof. dr. Lex Kaper

Examiners
Prof. dr. Lex Kaper
Prof. dr. Rudy Wijnands



**ANTON PANNEKOEK
INSTITUTE**

Abstract.

CONTEXT. High-Mass X-ray Binaries (HMXBs) provide an unique opportunity to determine their physical and orbital parameters with high precision, particularly when the system hosts an eclipsing X-ray pulsar. Previous studies have shown that OB supergiants in HMXBs exhibit luminosities that are *too high* for their masses.

AIMS. With new observational data and improved spectra, this research aims to better constrain the physical parameters of OB supergiants and confirm if these stars are *overluminous*.

METHODS. The luminosity (L) was calculated using photometry, distances from GAIA DR3, and the spectral types of the OB supergiants. The effective temperature (T_{eff}) was determined using two methods: one using spectral type - T_{eff} relations, and the other by fitting PoWR models to VLT/UVES and ESO/FEROS spectra. Using L and T_{eff} the black body radius was derived using $L = 4\pi R^2 \sigma T_{eff}^4$ and the expected mass was derived from its position in the Hertzsprung-Russell Diagram. From X-ray eclipse observations the eclipse radius was determined and the observed mass was determined from X-ray light curves and radial velocity measurements.

RESULTS. The values of L and T_{eff} obtained in this study differ from those reported in previous research, yet the OB supergiants still appear to be *overluminous* relative to their mass.

CONCLUSIONS. There does not seem to be a relation between the overluminosity of the OB supergiants and the mass transfer mechanism. Further research is needed to investigate the underlying reasons for this discrepancy.

Key words. X-rays: binaries – binaries: eclipsing – stars: early-type

1. Introduction

High-mass X-ray binaries (HMXBs) are among the brightest X-ray sources. These are systems that consist of a compact object, either a neutron star (NS) or a black hole (BH), orbiting a luminous and massive early B or O spectral type companion star, with a mass of $M \geq 8M_\odot$. The companion can be either a Be star or a supergiant. The HMXB phase is only a brief period in the evolution of these massive binaries, lasting only a few tens of millions of years. In these systems, X-ray radiation is generated by the accretion of matter from the companion star onto the compact object. As of now, there are 172 known HMXBs in the Milky Way (Neumann et al. 2023). HMXBs where the neutron star is a pulsar are particularly interesting because they offer an unique opportunity to measure the orbital and physical parameters of these system with very high accuracy.

In 1962, the first bright and persistent X-ray source beyond the solar system was discovered by a US *Aerobee* scientific suborbital sounding rocket with an X-ray instrument on board. The source, Sco X-1, is located in the Scorpius region with an X-ray luminosity of $L_X \sim 6 \times 10^4 L_\odot$ (Giacconi et al. 1962). Shortly after, it was proposed that the X-rays are possibly produced by the accretion of gas from a normal star onto a neutron star, within a close binary system. This was the discovery of the first X-ray binary. This discovery was not only the start of X-ray astronomy, but it also stimulated the multi-wavelength astronomy. And it marked the beginning of a new field in astrophysics, namely the domain of compact objects (i.e. neutron stars (NS) and black holes (BH)).

A few years after the discovery of Sco X-1, in 1964, Cygnus X-1 was discovered by another *Aerobee* rocket. The study of the optical counterpart revealed that it is in a binary system with the compact object. The study of the orbital parameters revealed that that the compact object has a mass of $M = 8.7 \pm 0.8 M_\odot$, which is much too heavy for a neutron star. Cyg X-1 thus became the first black hole orbiting a massive O9 star from which it is accreting. Making this the first discovered *High-Mass X-ray Binary* (HMXB) in our Galaxy (further reading Chaty 2022).

The evolution of massive binaries was first proposed by van den Heuvel & Heise 1972 (Figure 1). For a binary system to evolve into an HMXB, it must initially consist of two massive stars, each with a mass of $M \geq 12M_\odot$ by the time they reach the main sequence. During the evolution both stars can loose

mass due to mass transfer and end with less mass then at the start of the evolution. The more massive primary star evolves more rapidly and starts to expand. If the system is close enough it will eventually fill its Roche Lobe (RL) and start transferring mass to the less massive secondary star. The primary then goes supernova, leaving behind a compact object, either a black hole or a neutron star. If the secondary star is not ejected from the system, it will continue to evolve in the binary.

As the secondary star continues its evolution and reaches the supergiant phase, the system enters the HMXB phase. At this point, the strong stellar winds from the secondary star cause matter to be accreted onto the compact object, generating X-rays. When the secondary star eventually fills its own Roche lobe, it begins transferring mass directly onto the compact object, intensifying the X-ray emission due to increased accretion. Ultimately, the secondary star will also undergo a supernova. If the binary system is not disrupted, this results in a compact object binary that will eventually merge. This is a simplified overview of the evolution process; for a more detailed description, refer to Chaty 2022 or van den Heuvel & Heise 1972 .

During the HMXB phase, mass is transferred from the OB supergiant to the compact object, generating strong X-ray emission. This mass transfer can occur either through the strong stellar winds from the OB supergiant or via Roche-Lobe (RL) overflow. In wind-fed systems, the X-ray luminosity is typically around $L_x \sim 10^{35} \text{ erg s}^{-1}$, while in RL overflow systems, it is much higher, typically $L_x \sim 10^{38} \text{ erg s}^{-1}$ reaching the Eddington limit (Chaty 2022). Therefore, the X-ray luminosity can provide insights into the dominant mass transfer mechanism.

The spin period of the pulsar (P_s) also offers a way to distinguish between the mass transfer processes. In wind-fed systems, the spin period of the pulsar is usually on the order of minutes. However, in RL overflow systems, the pulsar spins up due to the transfer of not only mass but also angular momentum, leading to much shorter spin periods, typically ranging from seconds to milliseconds. Additionally, in RL overflow systems, the OB supergiant co-rotates with the orbit. The drag caused by the RL overflow gradually synchronizes the rotation period of the OB supergiant with the orbital period of the system.

HMXBs are very interesting to study because the X-ray pulsar within the system offers a unique opportunity to determine the orbital and physical parameters with great accuracy through

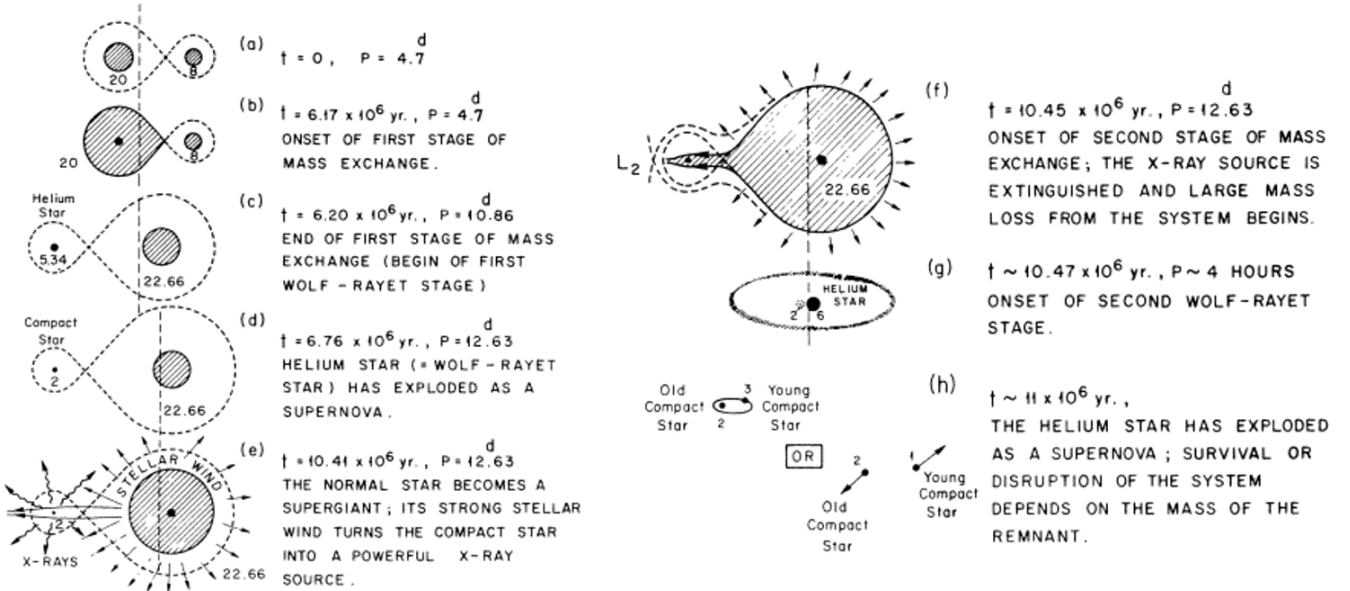


Fig. 1: Evolution of massive binaries as first proposed by [van den Heuvel 1976](#).

pulsar timing analysis. As the pulsar orbits the companion star, it moves closer and farther from the observer, causing variations in the arrival times of its pulses. These arrival times show a sine-like pattern, from which parameters such as the orbital period, projected semi-major axis, radial velocity, eccentricity and even the rate of change in the orbital period can be derived. When these parameters are combined with radial velocity measurements of the companion, the mass of both stars can be derived relative to the inclination.

However, since the inclination of the orbit is usually unknown, some parameters can only be constrained relative to the inclination. This issue can be solved by studying eclipsing systems, where the inclination is typically $i \gtrsim 67^\circ$, allowing for a better constraint of these parameters. Additionally, the X-ray eclipse enables highly accurate measurements of the radius of the OB supergiants. The combination of the X-ray pulsar and the eclipse enables us to measure the orbital and physical parameters of these systems with very high accuracy.

Earlier studies by [Conti 1978](#) and [Kaper 2001](#) suggested that the OB supergiants in HMXBs appear to be too luminous for their mass. This discrepancy is illustrated in figure 2 from [Kaper 2001](#), where the HMXB Cen X-3 (amongst others) is shown on a Hertzsprung-Russell Diagram. The system contains an O6.5III supergiant with a measured mass of $19M_\odot$, but its luminosity indicates it should have a mass of $50M_\odot$. This inconsistency suggests that the star is either *overluminous, undermassive* or both. Additionally, the black-body radius corresponding to a star with a mass of $50M_\odot$ is larger than the measured eclipse radius of this supergiant (figure 2b), implying that the star also is *undersized*. This behaviour is very unusual since it should not matter what method is used for determining these parameters. If this phenomenon is real, it indicates that we may not fully understand the evolution of stars in binary systems.

The goal of this research is to revisit these stellar parameters and confirming if the *overluminosity* of these OB supergiants is real. Compared to [Conti 1978 & Kaper 2001](#) there are now much better measurements available. With the release of GAIA DR3, we now have access to highly accurate distance measurements, which are crucial for determining the luminosity of these stars. Additionally, VLT/UVES and ESO/FEROS

spectra are available, allowing for more precise classification of the spectral types of the OB supergiants and improved determination of their effective temperatures. Furthermore, the X-ray light curves from IBIS/ISGRI and RXTE/ASM, spanning nearly two decades, give us more accuracy on the radius of these stars ([Falanga et al. 2015](#)).

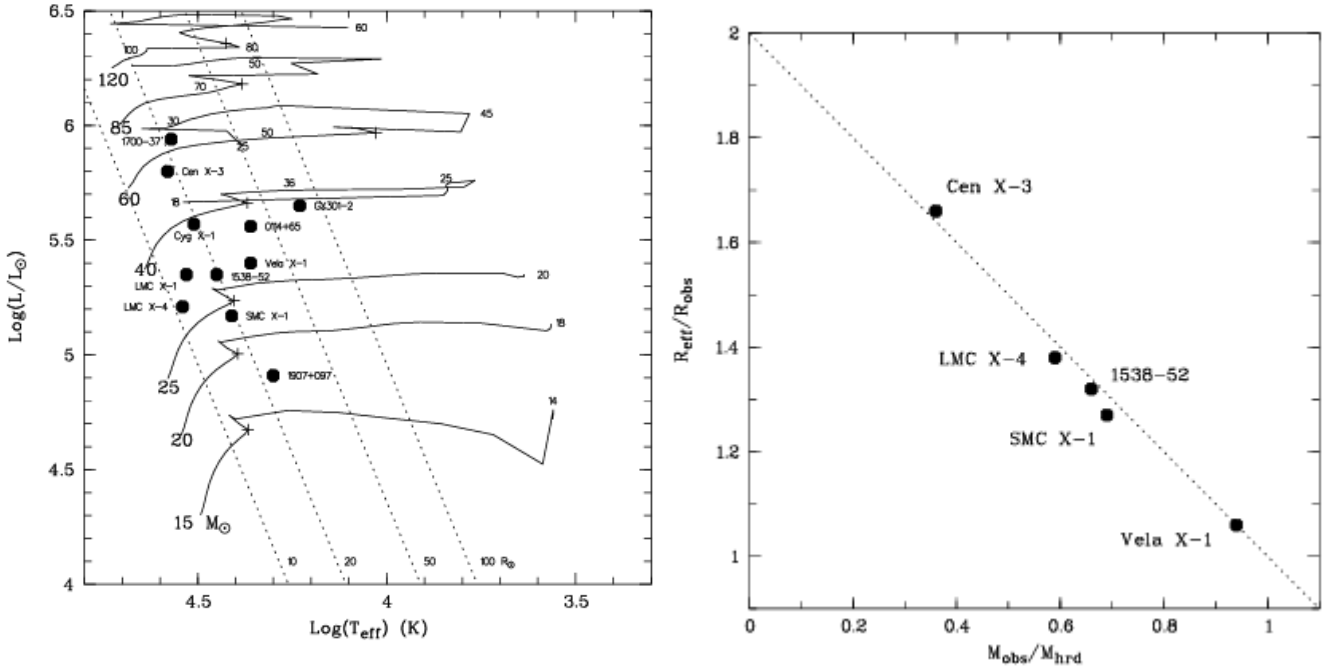
The remainder of this paper is organized as follows: section 2 discusses the data and the sample of high-mass X-ray binaries (HMXBs). Section 3 covers the recalculation of the parameters. The results are presented in section 4, followed by a discussion in section 5 and conclusion in section 6.

2. Data & Objects

The goal of this research is to revisit the physical parameters calculated by [Kaper 2001](#) and to confirm whether the *overluminosity* of the optical stars in HMXBs is real. To achieve this, the HMXB systems studied must meet specific criteria. Firstly, the system must be eclipsing, as this allows for accurate measurements on the radius of the OB supergiant and provides a constraint on the inclination, which is an essential factor for determining the mass of the optical star. Additionally, if the system includes an X-ray pulsar, X-ray pulse timing delay measurements can be performed, which offer very accurate constraints on the orbital and physical parameters of the system.

Currently, there are 172 known HMXBs in the Milky Way ([Neumann et al. 2023](#)), of which only 42 are confirmed to host an OB supergiant. Furthermore, there are 9 eclipsing HMXBs and of these systems only 5 host an OB supergiant and an X-ray pulsar. An up-to-date catalogue of Galactic HMXBs can be found on [HMXB catalogue](#) ([Neumann et al. 2023](#)).

[Falanga et al. 2015](#) conducted Monte Carlo simulations on the X-ray light curves for 8 of these eclipsing HMXBs (including two from the Magellanic Clouds). They utilized X-ray data from IBIS/ISGRI onboard the ESA/INTEGRAL mission (light curves dating back to 2003) and the All Sky Monitor (ASM) onboard RXTE (light curves since 1996). Along with radial velocity measurements of both objects, they were able to determine the mass and radius of the OB supergiants, along with the orbital parameters of the systems.



(a) HRD diagram with HMXB data from Kaper 2001 . The solid lines are evolutionary tracks (Lejeune & Schaerer 2001) and the numbers indicate the masses during the evolution. The dotted lines are the lines of constant radius.

(b) Fractions of expected and measured masses and radii for five HMXBs. For the optical stars the expected mass (M_{hrd}) is derived from the position in the HRD and the black body radius (R_{eff}) derived from $L = 4\pi R^2 \sigma_{sb} T_{eff}^4$. The observed radius (R_{obs}) is determined from X-ray eclipse measurements and the observed mass (M_{obs}) using X-ray pulse timing delay measurements and radial velocity measurements. The dotted line is not a fit, but implies a possible relation between the two fractions.

Fig. 2: Results from Kaper 2001 .

Table 1: HMXB sample. The distances are from Bailer-Jones et al. 2021 . The spectral type of the OB supergiants, orbital period ($P_{orb,ecl}$) and pulse period of the X-ray pulsar (P_s) are from Falanga et al. 2015 .

id	ID Optical	Spec. Type	$d [kpc]$	$P_{orb,ecl} [d]$	$P_s [s]$
4U1538-52	QV Nor	B0.2Ia	$5.54^{+0.35}_{-0.44}$	3.72841	526.8
4U1700-37	HD 153919	O6.5Iaf+	$1.51^{+0.08}_{-0.05}$	3.41158	–
Cen X-3	V779 Cen	O6.5III	$6.75^{+0.68}_{-0.46}$	2.08704	4.8
LMC X-4	LMC X-4	O8III	$48.59^{+4.0}_{-4.0}$	1.40838	13.5
SMC X-1	Sk 160	B0Ib	$62.44^{+4.0}_{-4.0}$	3.89192	0.71
Vela X-1	HD 77581	B0.5Iae	$1.97^{+0.06}_{-0.07}$	8.96443	283.2

For the luminosity a number of parameters is needed. A very crucial parameter is the distance, which is now very well known with the parallaxes from GaiaDR3 . Bailer-Jones et al. 2021 have used these Gaia data to determine the distances towards the systems. However, due to the very small parallax values for objects in the Small Magellanic Cloud (SMC) and the Large Magellanic Cloud (LMC), the distance measurements to these galaxies come with high uncertainties. For this reason, the distances to SMC X-1 and LMC X-4 from Graczyk et al. 2020 and Pietrzyński et al. 2019 , respectively are used, with the depth of these galaxies (Subramanian & Subramaniam 2009) as the associated error.

In addition, photometric data is needed. In HMXBs the measured magnitude of the optical star is not constant due to ellipsoidal variations. Due to tidal distortions from the compact

object, the optical star gets stretched along the direction of the compact object, resulting that the surface observed by the observer is not constant over the period of the system. Therefore light curves of the OB supergiants are needed to get the correct magnitudes in the Johnson V and B band. An example of such a light curve is shown in figure 4 for Cen X-3 (Krzeminski 1974). The magnitude taken is the average of all magnitudes measured. All photometric data is listed in table 3.

Finally, high resolution spectra are needed to check the spectral types and determine the effective temperature of the optical stars. These spectra are provided by VLT/UVES and ESO/FEROS from the ESO archive. Details of the spectra are listed in table 2 and multiple sections are plotted in figure 3.

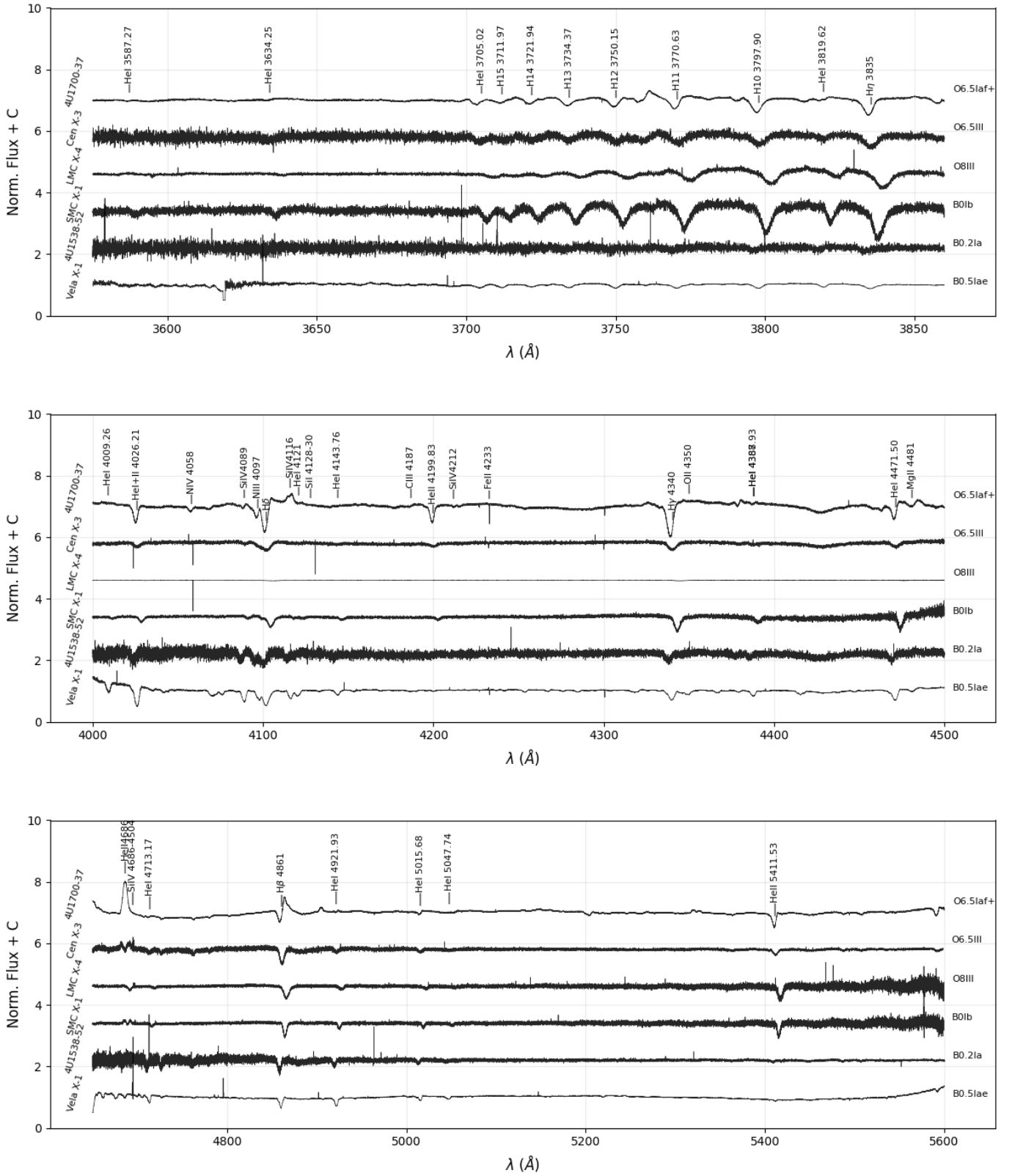


Fig. 3: Normalized UVES & FEROS (for *Vela X-1*) spectra. Important spectral lines are annotated.

2.1. Sample

Based on the requirements described above, 6 eclipsing HMXBs are selected. In this section I will introduce the systems and re-

view the spectral types using criteria from [Liu et al. 2019](#). Note: All spin periods, orbital periods and spectral types below are from [Falanga et al. 2015](#).

Table 2: UVES & FEROS spectra details.

id	ID Optical	Orbital Phase	T_{obs} [MJD]	λ_{min} [\AA]	λ_{max} [\AA]	SNR	R	Instrument
4U1538-52	QV Nor	0.007	55297.195	3282.031	4563.057	9.096	49620	UVES
4U1538-52	QV Nor	0.007	55297.195	4583.137	6686.554	63.756	51690	UVES
4U1700-37	HD 153919	0.002	57576.029	3044.237	3916.668	116.187	71050	UVES
4U1700-37	HD 153919	0.002	57576.029	4583.091	6686.474	330.342	107200	UVES
Cen X-3	V779 Cen	0.740	52328.232	4583.455	6686.468	90.712	42310	UVES
Cen X-3	V779 Cen	0.740	52328.232	3281.074	4562.458	32.821	40970	UVES
LMC X-4	LMC X-4	0.419	52245.202	3281.097	4562.446	59.574	40970	UVES
LMC X-4	LMC X-4	0.420	52245.203	4583.488	6686.490	64.836	42310	UVES
SMC X-1	Sk 160	0.543	52187.146	3281.079	4562.432	50.243	40970	UVES
SMC X-1	Sk 160	0.544	52187.147	4583.488	6686.489	69.823	42310	UVES
Vela X-1	HD 77581	0.440	59934.376	3527.790	9217.320	377.900	48000	FEROS

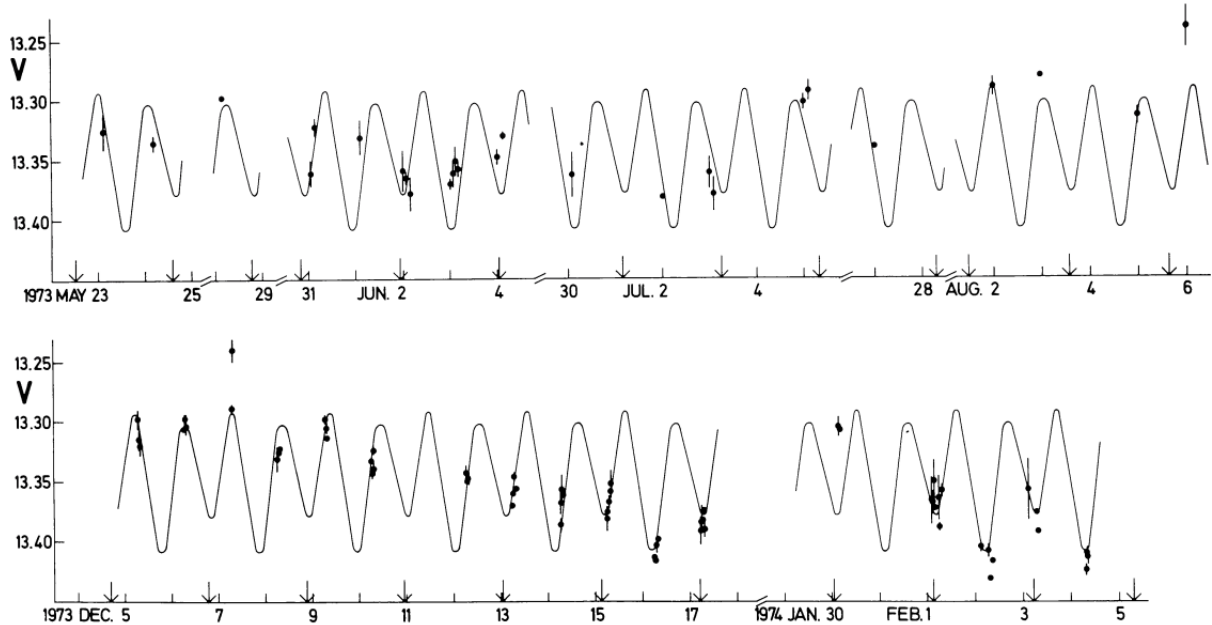


Fig. 4: (Source: [Krzeminski 1974](#)) Visual light curve of the optical companion to Cen X-3 in the V-band. The solid curve is a freehand smoothed fit.

4U1538-52 is a bright HMXB hosting a 526s X-ray pulsar orbiting OB supergiant QV Nor in an orbital period of 3.73d. QV Nor has visual magnitude $V = 14.35$ ([Pakull et al. 1983](#)) and spectral type $B0.2Ia$. The spectrum of QV Nor shows no presence of the HeII 4200 Å line, but there is a weak HeII 4686 Å line, alongside absorption in SiIV 4089 Å. Based on these spectral features, a classification as $B0$ is plausible.

4U1700-37 does not host an X-ray pulsar, which leads to higher uncertainties in the determination of its orbital and physical parameters compared to other systems. The system hosts the O6.5Iaf+ supergiant HD 153919, with a visual magnitude of 6.54 ([Bolton & Herbst 1976](#)). The UVES spectrum contains HeII 4686 Å in emission, along with a P Cygni profile for H β 4861 Å. These spectral features indicate the presence of dense and strong stellar winds, suggesting a high luminosity. The UVES spectrum also shows the lines HeI+II 4026 Å and HeII 4200 Å, where the equivalent width of HeI+II 4026 Å is slightly larger than that of HeII 4200 Å. Additionally, SiIV 4089 Å is

weakly present, suggesting that the spectrum corresponds to an O6 type star.

Cen X-3 was the first binary discovered with an X-ray pulsar ([Giacconi et al. 1971](#); [Schreier et al. 1972](#)). Mass is transferred onto the compact object via RL overflow causing the pulsar to spin-up and having a spin period of 4.8s. The optical star V779 Cen has a visual magnitude of $V = 13.35$ ([Krzeminski 1974](#)) and spectral type O6.5III. The UVES spectrum contains HeI+II 4026 Å and HeII 4200 Å where the equivalent width of HeI+II 4026 Å is slightly larger than HeII 4200 Å, which is typical for an O6 type star.

LMC X-4 is a HMXB in the Large Magellanic Cloud containing a 13.5s X-ray pulsar that orbits the optical star in a period of 1.41d. Mass is transferred via RL overflow. The optical star has a visual magnitude of $V = 14$ ([Ilovaisky et al. 1984](#)) and spectral type O8III. The equivalent width of HeI+II 4026 Å is greater than HeII 4200 Å, meaning a spectral type of O6 or later.

There is weak SiIV 4089 Å and no SiIV4116 Å. So a spectral type of *O*8.

SMC X-1 is a HMXB in the Small Magellanic Cloud containing a sub-second X-ray pulsar with a spin period of 0.71s. Mass from the optical star is transferred via RL overflow onto the compact object. The optical star SK 160 has a visual magnitude of $V = 13.15$ (Massey 2002) and spectral type B0Ib. The UVES spectrum contains weak HeII 4200 Å and HeII 4686 Å. There is weak NIII 4634-40-42 emission and SiIV 4089 and SiIV4116 absorption. Based on the table in Liu et al. 2019 these lines are typical for a *B0* type star.

Vela X-1 is a wind-fed system with a 283.2s X-ray pulsar. The optical star has a visual magnitude of $V = 6.87$ (Cherepashchuk 1982) and spectral type B0Iae. The UVES spectrum contains weak HeII 4200 Å and HeII 4686 Å. Based on the table in Liu et al. 2019 these lines correspond to a *B0* type star.

3. Revisiting parameters

In this section the methods used and the obtained results of determining the physical parameters of the OB supergiants will be described. As described in section 1 the luminosity of the optical stars is too high for their mass, or vice versa, based on data from Kaper 2001. Additionally, the radius calculated from the luminosity does not match the actual radius measured from X-ray eclipses. Therefore, the key parameters to determine are the luminosity and effective temperature, which are used to estimate the expected mass and radius, as well as the 'real' mass and radius obtained from the eclipse, X-ray pulse timing measurements and radial velocity measurements. The latter has already been determined by Falanga et al. 2015.

3.1. Luminosity

Determining the luminosity of the OB supergiants involves parameters that require careful consideration, although the calculation is mathematically straightforward. The luminosity of a star can be calculated using the *bolometric luminosity equation*

$$L = 10^{\frac{M_{bol}-4.74}{-2.5}} L_{\odot} \quad (1)$$

where L is the luminosity in solar luminosities (L_{\odot}) and M_{bol} the bolometric magnitude in *mag*. The M_{bol} can be determined using

$$M_{bol} = M_V + BC_V \quad (2)$$

where, M_V is the absolute magnitude in photometric passband V in *mag* and BC_V the bolometric correction for the V passband in *mag*. Note: the photometric passband can be any other one, but since I used the Johnson V band I will use it here for clarity.

At this stage, two parameters remain unknown: the bolometric correction BC_V and the absolute magnitude M_V . The bolometric correction BC_V is derived from existing relations. For O-type stars, the BC_V - spectral type relation from Martins & Plez 2006 is used, which distinguishes between different luminosity classes (I, III, V) (table A.1). To get the corresponding BC_V , the spectral types from table 1 are used. For B-type supergiants, the BC_V - effective temperature relation from Crowther et al. 2006 is applied, given by

$$BC_V = 20.15 - 5.13 \times \log(T_{eff}) \quad (3)$$

where T_{eff} is the effective temperature in K . The effective temperature based on spectral type in table 5 is used (see section 3.2).

The absolute magnitude M_V can be calculated using the *distance modulus*:

$$M_V = m_V - 5 \log(d) + 5 - A_V \quad (4)$$

where m_V is the visual magnitude in passband V in *mag*, d the distance to the star in *pc* and A_V the interstellar extinction in passband V in *mag*. The distances (from Bailer-Jones et al. 2021) and visual magnitudes from table 3 are used for the calculation.

This leaves the extinction parameter A_V . Determining the extinction is less straightforward and requires certain assumptions. The extinction can be estimated by comparing the observed color index $(B - V)_{obs}$ with the expected intrinsic color index $(B - V)_0$ from stellar models and assuming an extinction coefficient that is constant throughout the galaxy R_V :

$$A_V = R_V \times [(B - V)_{obs} - (B - V)_0] \quad (5)$$

where A_V is the extinction in the V-band in *mag*, R_V the extinction coefficient in the V-band, $(B - V)_{obs}$ the observed color index in *mag* and $(B - V)_0$ is the intrinsic color index *mag* derived from stellar models based on the spectral type of the optical star. For $(B - V)_0$ the color - spectral type relations are used from Martins & Plez 2006 (table A.1), the observed colors are displayed in table 3 and for R_V different values are used for the Milky Way and both Magellanic Clouds. The following values are used, $R_V = 3.16$ for the Milky Way (Wang & Chen 2019), towards the LMC $R_V = 3.4$ and for the SMC $R_V = 2.53$ (Wang & Chen 2023).

Results of the luminosity are listed in table 4.

3.2. Effective Temperature

In this section two methods will be discussed for determining the effective temperature: one based on a relation between the effective temperature and the spectral type of the optical star and the other by fitting model spectra to spectra of the optical stars.

3.2.1. Spectral type - T_{eff} relation

The effective temperature can be determined using relations with the spectral type of the OB supergiants. For O-type stars, parameters from Martins et al. 2005 were used (table A.1), and for B-type stars the T_{eff} comes from Zorec et al. 2009. Results are listed in table 5 under *Spec. Type*.

3.2.2. PoWR model fit

The Potsdam Wolf-Rayet Models provide grids of model spectra for O and B-type stars with solar metallicity for stars in the Milky Way and $\frac{1}{2}$ & $\frac{1}{7}$ solar metallicities for the LMC & SMC respectively. Each grid has a 2-dimensional parameter space, the effective temperature and surface gravity ($\log(g)$ [cm s^{-2}]). The effective temperature ranges from 15 – 56 kK for the Milky Way and from 15 – 50 kK for the LMC and SMC and the surface gravity ranges from 2.0 – 4.4 ($\log(g)$). Figure 5 shows an example of these models spectra for HeII 4200 Å.

With these models the T_{eff} and $\log(g)$ of the optical stars can be determined by overlaying the models over the spectra. The model that deviates the least from the spectrum gives the best estimation of the two parameters.

Table 3: Photometric data. The parameters are compared with data from Kaper 2001 .

id	Spec. Type	<i>V</i>		B-V		$(B - V)_0$		BC_V		$d [kpc]$	
		<i>This work</i>		<i>Kaper 2001</i>		<i>This work</i>		<i>Kaper 2001</i>		<i>This work</i>	
		<i>This work</i>	<i>Kaper 2001</i>	<i>This work</i>	<i>Kaper 2001</i>	<i>This work</i>	<i>Kaper 2001</i>	<i>This work</i>	<i>Kaper 2001</i>	<i>This work</i>	<i>Kaper 2001</i>
4U1538-52	B0.2Ia	14.35	14.40	1.97	1.90	-0.26	-0.20	-2.32	-2.49	$5.54^{+0.35}_{-0.44}$	6.40
4U1700-37	O6.5Iaf+	6.54	6.60	0.25	0.27	-0.27	-0.25	-3.32	-3.70	$1.51^{+0.08}_{-0.05}$	1.90
Cen X-3	O6.5III	13.35	13.30	1.07	1.07	-0.27	-0.33	-3.42	-3.70	$6.75^{+0.68}_{-0.46}$	10.00
LMC X-4	O8III	14.00	14.00	-0.23	-0.10	-0.27	-0.20	-3.16	-3.40	$48.59^{+4.0}_{-4.0}$	52.00
SMC X-1	B0Ib	13.15	13.30	-0.15	-0.14	-0.26	-0.17	-2.35	-2.49	$62.44^{+4.0}_{-4.0}$	60.00
Vela X-1	B0.5Iae	6.87	6.90	0.50	0.47	-0.26	-0.23	-2.16	-2.10	$1.97^{+0.06}_{-0.07}$	1.90

^a Kaper 2001

^b Massey 2002

^c Illovaisky et al. 1984

^d Cherepashchuk 1982

^e Krzeminski 1974

^f Pakull et al. 1983

^g Bolton & Herbst 1976

Table 4: Luminosity results.

id	Spec. Type	$L[L_\odot](10^5)$	
		<i>This work</i>	<i>Kaper 2001</i>
4U1700-37	O6.5Iaf+	$4.3^{+0.6}_{-0.5}$	8.7
Cen X-3	O6.5III	$2.0^{+0.4}_{-0.3}$	6.3
LMC X-4	O8III	$1.0^{+0.2}_{-0.2}$	1.6
SMC X-1	B0Ib	$1.9^{+0.3}_{-0.3}$	1.5
4U1538-52	B0.2Ia	$2.7^{+0.5}_{-0.5}$	2.2
Vela X-1	B0.5Iae	$3.7^{+0.4}_{-0.4}$	2.5

To compare the models with the data, a number of spectral lines is selected from the UVES and FEROS spectra (table 2). For OB stars the most temperature sensitive spectral lines are HeII, HeI, SiIII and SiIV. The wings of the Balmer lines are more sensitive for different surface gravities and are best for fitting $\log(g)$. Per object, the spectral lines are selected and individually normalized. This is done by selecting continuum from the surrounding spectrum by hand and fit a 3 dimensional polynomial through the continuum (example in figure 6).

Before comparing the model to the data, corrections for the radial velocity (Doppler shift) and the rotation of the star (Doppler broadening) must be applied. The radial velocity v_r of the system is determined by fitting a Gaussian to a series of spectral lines (see figure B.1). The average of these fits is taken as the radial velocity, with the uncertainty estimated as the standard deviation (1σ) for all lines. The rotational velocity of the star ($v \cdot \sin(i)$) is treated as a free parameter and incorporated into the model grid (bottom panel of Figure 5).

Now a grid search can be performed. For every T_{eff} , $v \cdot \sin(i)$ and $\log(g)$ the deviation from the data is calculated with

$$\chi^2_{red} = \frac{1}{N_{lines}} \sum_{i=0}^{N_{lines}} \frac{1}{N_i} \sum_{j=0}^{N_i} \left(\frac{\mathcal{F}_{obs}^{ij} - \mathcal{F}_{mod}^{ij}}{\mathcal{E}_{obs}^{ij}} \right)^2 \quad (6)$$

where N_{lines} is the number of spectral line selected from the spectrum, N_i the number of flux points for the i^{th} spectral line, \mathcal{F}_{obs}^{ij} the normalized flux of the data, \mathcal{F}_{mod}^{ij} the flux of the model and \mathcal{E}_{obs}^{ij} the SNR $^{-1}$ of the spectrum containing the line. Before χ^2 is calculated the model is corrected for the radial velocity. For every value of $v \cdot \sin(i)$ the model is broadened using the *rotBroad* function from the PyAstronomy package.

For each free parameter the $\frac{1}{\chi^2_{red}}$ is plotted for each model (figure 7). The errors on the parameters are determined as described in Tramper et al. 2014. First the best-fitting model must be identified, which is the model with the lowest χ^2 value. Second, all χ^2 values must be multiplied by a factor that the χ^2_{red} of the best model equals unity. This is equivalent to dividing all χ^2 values by the χ^2_{red} of the best model.

Next, models that are statistically indistinguishable from the best model must be identified. This is done by calculating the probability P that the difference between two models is caused by random fluctuations:

$$P = 1 - \Gamma(\chi^2/2, \nu/2) \quad (7)$$

with $\Gamma(\chi^2/2, \nu/2)$ the incomplete gamma function, representing the cumulative distribution function of the χ^2 distribution, evaluated at χ^2 , for $\nu = n_{data} - n_{free}$ the degrees of freedom. Here n_{data} is the number of flux points taken taken into account during the fit and n_{free} the number of free parameters. The models that fit best are those with $P > 0.05$, corresponding to the 95% confidence interval. In figure 7, this confidence interval is indicated by the orange dotted lines, while the solid orange line represents the best-fitting parameter.

The fit results are displayed in table 5, together with the effective temperatures based on spectral type. In appendix C, the fit results are individually shown per object.

3.3. Radius

Using the luminosity and effective temperature, the radius of the star can be calculated. Alternatively, the radius can also be determined using X-ray eclipse measurements. As highlighted in section 1, these radii do not seem to agree and the optical stars in HMXBs appear to be *undersized*. This section will discuss both methods for determining the radius.

3.3.1. Black body radius R_{eff}

Using the luminosity and the effective temperature, the radius of a star can be calculated using

$$R_{eff} = \sqrt{\frac{L}{4\pi\sigma T_{eff}^4}} \quad (8)$$

where L is the luminosity in $J \cdot s^{-1}$, T_{eff} the effective temperature in K and σ the Stefan-Boltzmann constant. To calculate the

Table 5: Results of effective temperatures (T_{eff}) and fit parameters. The T_{eff} under *Spec. Type* are based on the spectral types of the OB companions (section 3.2.1). The parameters under *Model Fit* are from the PoWRmodel fits on UVES and FEROS spectra (section 3.2.2).

id	Spec. Type		Model Fit			
	T_{eff} [K]	T_{eff} [K] Kaper 2001	T_{eff} [K]	$\log(g)$ [cgs]	$v \cdot \sin(i)$ [km s $^{-1}$]	v_r [km s $^{-1}$]
4U1538-52	24000	28000	28000 ± 2000	3.2 ± 0.2	140^{+20}_{-18}	-166 ± 12
4U1700-37	35895	37200	32000	3.2	240^{+18}_{-30}	-50 ± 24
Cen X-3	34500	38000	27000	3.2	220^{+20}_{-20}	1 ± 12
LMC X-4	32573	35000	31000	3.4	260^{+10}_{-10}	315 ± 18
SMC X-1	24380	26000	23000 ± 2000	2.8 ± 0.2	170^{+18}_{-18}	188 ± 5
Vela X-1	22370	22900	25000	2.8	150^{+10}_{-0}	-19 ± 6

radius, the luminosity as described in section 3.1 and the effective temperature based on the spectral type as outlined in section 3.2.1 are used. The resulting radii are presented in table 6.

3.3.2. Eclipse radius R_{ecl}

The six HMXBs analyzed in this research are all eclipsing binaries, providing a unique opportunity to accurately measure the radius of the OB companions by determining the eclipse angle. Because the compact objects primarily emit X-rays, the eclipse duration is best measured using X-ray data. This measurement has been done by Falanga et al. 2015 , who utilized X-ray light curves from the ASM and IBIS/ISGRI instruments to determine the radii of the OB companions. These radii are presented in table 6.

Table 6: Results of the eclipse radius (R_{ecl}) from Falanga et al. 2015 and the black body radius (R_{eff}) based on the luminosity (section 3.1 and effective temperature (section 3.2.1) using equation 8.

id	R_{ecl} [R_\odot]		R_{eff} [R_\odot]		
	id	This work	Kaper 2001	This work	Kaper 2001
4U1538-52	13.0 ± 1.0	15	$29.8^{+3.6}_{-3.9}$	20.1	
4U1700-37	22.0 ± 2.0	22	$17.0^{+1.5}_{-1.4}$	22.5	
Cen X-3	11.4 ± 0.7	11	$12.5^{+1.6}_{-1.3}$	18.3	
LMC X-4	7.4 ± 0.4	8	$9.8^{+1.1}_{-1.1}$	11.0	
SMC X-1	15.0 ± 1.0	15	$24.4^{+2.8}_{-2.8}$	19.0	
Vela X-1	29.0 ± 1.0	30	$40.7^{+4.3}_{-4.3}$	31.8	

3.4. Mass

Using the luminosity and effective temperature, the mass of the optical stars can be determined based on its position in the HRD. Alternatively, the mass can also be determined using X-ray pulse timing delay measurements, X-ray light curves and radial velocity measurements. This section will discuss both methods for determining the mass.

3.4.1. Expected mass M_{HRD}

To estimate the mass of the OB stars based on their luminosity (L) and effective temperature (T_{eff}), evolutionary tracks from Chen et al. 2015 were plotted on a Hertzsprung-Russell diagram alongside the observational data (figure 9). The luminosity values were derived from the photometric data, as discussed in section 3.1, and the effective temperature was determined based on the spectral type, as described in section 3.2.1. The diagram includes mass labels corresponding to various stages of stellar evolution. The mass of each OB star was manually estimated by locating its position on the diagram, with an estimated accuracy of approximately 2 solar masses. These results are presented in Table 7.

3.4.2. Observed mass M_{obs}

The masses of the optical stars are determined by Falanga et al. 2015 . They applied Monte-Carlo simulations on folded light curves form IBIS/IGRI and ASM data in combination with radial velocity measurements of the X-ray pulsar and optical companion. The masses they obtained are presented in table 7.

Table 7: Results of the expected mass based on the positions in the Hertzsprung Russell Diagram (figure 9) and the observed mass by Falanga et al. 2015 .

id	M_{OB} [M_\odot]		M_{HRD} [M_\odot]		
	id	This work	Kaper 2001	This work	Kaper 2001
4U1538-52	16	16 ± 2	16	29 ± 2	24
4U1700-37	46	46 ± 5	52	41 ± 2	60
Cen X-3	24	24 ± 1	18	29 ± 2	50
LMC X-4	18	18 ± 1	16	22 ± 1	25
SMC X-1	18	18 ± 2	17	23 ± 2	23
Vela X-1	26	26 ± 1	24	32 ± 2	23

4. Results

The determined luminosities are presented in Table 4 and compared with the luminosities reported by Kaper 2001 . For the O-type stars, the luminosities decrease as the spectral type progresses to later types, as one would expect. However, this trend

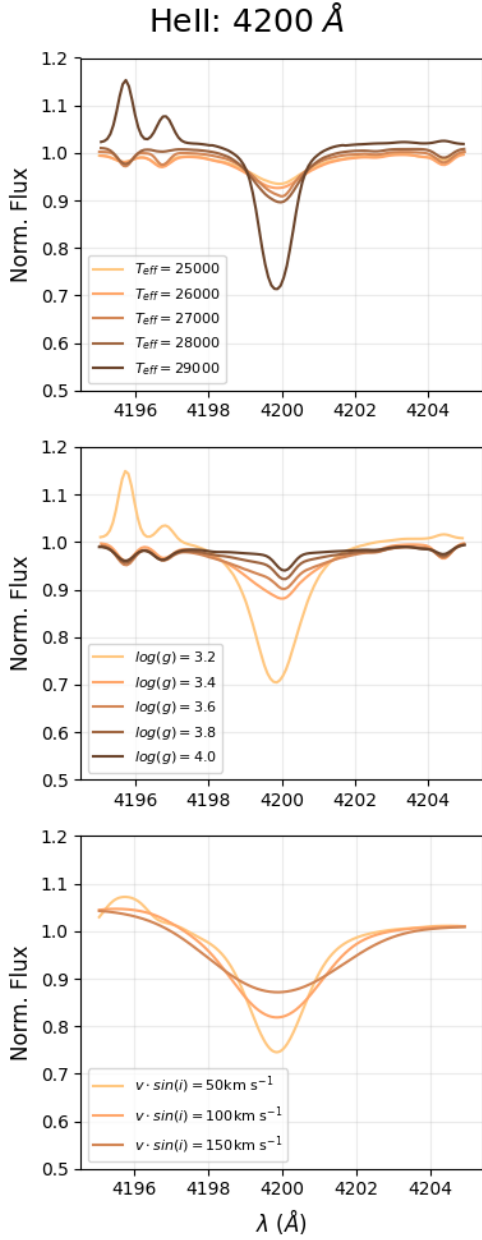


Fig. 5: Small selection of the PoWRmodels (Hainich et al. 2019). The HeII 4200 Å line is plotted in the 3 panels. On the x-axis is the wavelength in Angstrom(Å) and on the y-axis the normalized flux. *Top:* Models for different effective temperatures with constant $\log(g) = 3.0$ and $v \cdot \sin(i) = 0 \text{ km s}^{-1}$. *Middle:* Models for different surface gravities with constant $T_{\text{eff}} = 30000K$ and $v \cdot \sin(i) = 0 \text{ km s}^{-1}$. *Bottom:* Models for different rotational velocities with constant $T_{\text{eff}} = 30000K$ and $\log(g) = 3.2$.

does not hold for the B-type stars, with *Vela X-1* in particular having a significantly higher luminosity than what would be expected for its spectral type. When comparing these results to those obtained by Kaper 2001 , noticeable differences are observed for some objects. For instance, the luminosity of *Cen X-3* differs by a factor of approximately 3 from the values reported in the previous study.

The effective temperatures determined by the two methods are summarized in Table 5. It is notable that the temperatures based on spectral type, as derived in this study, are generally lower for all OB supergiants compared to those reported by Kaper 2001 . The results from the spectral model fits, also shown in Table 5, indicate significant deviations for some objects. In particular, *Cen X-3* exhibits a temperature that is 7500K lower than derived from the spectral type.

The eclipse radius and black body radius results are shown in table 6. The radii obtained from X-ray eclipse measurements are consistent with the values reported by Kaper 2001 , showing no significant deviation. However, the radii calculated using the black body model exhibit larger discrepancies, with differences reaching up to a factor of 1.5. This is consistent with the variations observed in luminosity and effective temperature, which also show significant deviations from previous values.

Finally, the results for the expected and observed masses are presented in table 7. The observed masses generally align with those reported by Kaper 2001 , with the notable exception of *Cen X-3*, where the mass is found to be 6 solar masses higher. The expected masses show deviations of up to a factor of 1.5. These differences are consistent with the variations observed for the luminosity and effective temperature, which also differ significantly from previous measurements.

5. Discussion

As discussed in section 4, the luminosities determined in this work differ significantly from those reported by Kaper 2001 . The primary explanation for these discrepancies lies in the differences in distance measurements. With the new data from GaiaDR3 , distances are now much better constrained. For example, the distance to *Cen X-3* is now determined to be 3250 pc closer compared to the value used by Kaper 2001 , which mostly explains why the luminosity calculated in this work is three times lower.

Another contributing factor to the differences in luminosity is the bolometric correction (BC_V). The bolometric corrections applied in this work are generally higher compared to those used by Kaper 2001 . The BC_V is significantly higher for 4U1700-37 (~ 0.4 mag), leading to a lower luminosity in this study. While the V and B magnitudes also differ slightly, these differences are not significant. Therefore, the primary reasons for the differences in luminosities are the bolometric corrections and the updated distance measurements.

Additionally, the interstellar extinction was calculated using an extinction coefficient (R_V) that is assumed to be constant throughout the galaxies, which may not accurately reflect the varying conditions across different regions. This assumption could have introduced some inaccuracies in the luminosity measurements.

The effective temperatures obtained from the model fits do not consistently align with those determined from the spectral type of the OB supergiants (table 5). For 4U1700-37 and *Vela X-1*, the distribution of the χ^2 values do not show a smooth rise to a well-defined maximum followed by a descent (figure 7), instead, it displays irregular spikes. Consequently, it is not trivial to say which model best describes the data. This inconsistency is likely due to the normalization process. The spectra of these objects display significant patterns in the continuum, complicating the selection of appropriate continuum regions.

For the other four objects, the χ^2 distribution show fewer of these random spikes, indicating a more stable fit. However, it

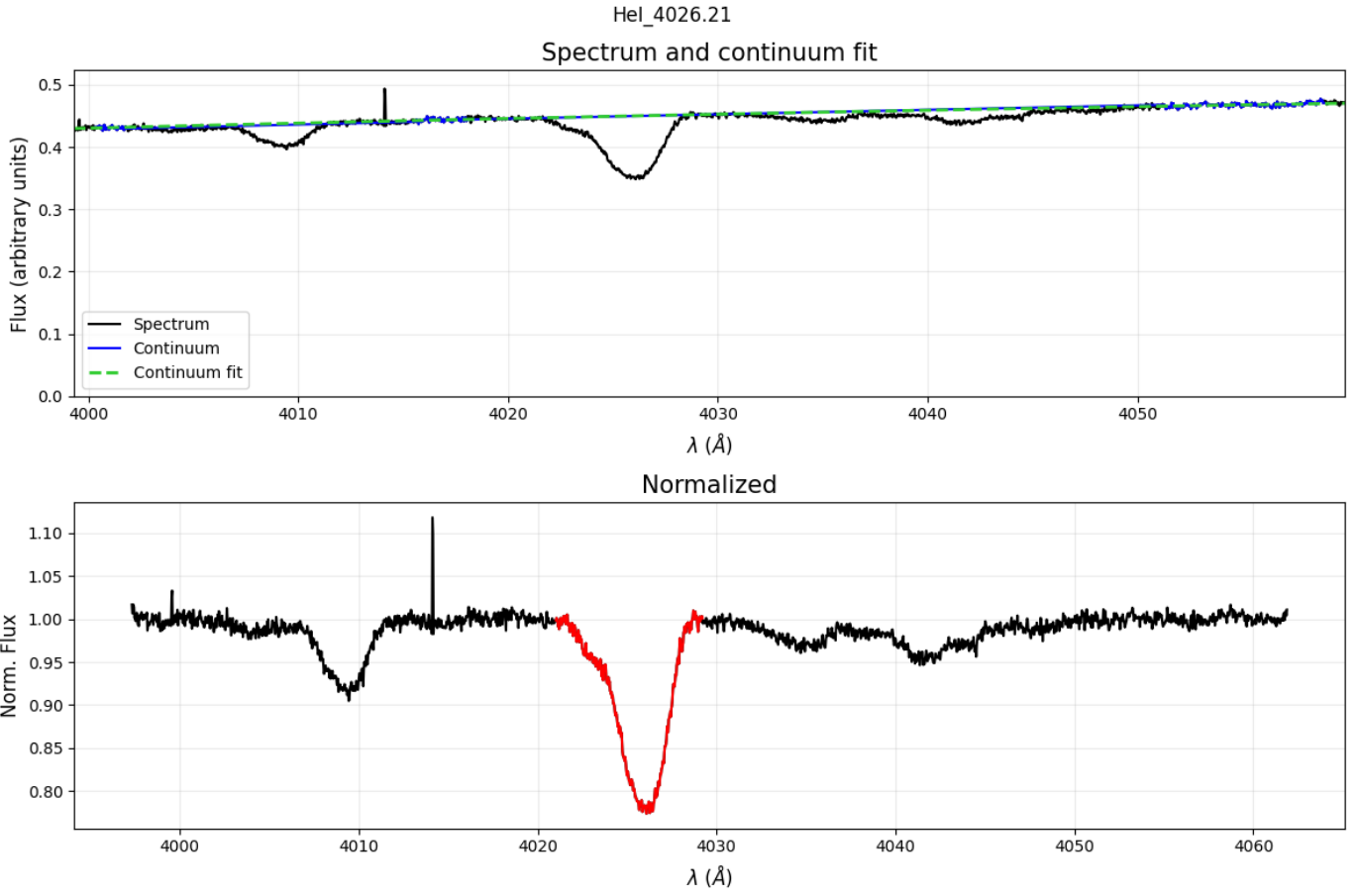


Fig. 6: Example of normalizing a spectral line, in this case for HeI 4026.21 Å in the FEROS spectrum for Vela X-1. *Top:* The continuum is manually selected from the spectrum (blue parts). The green line is a 3rd order polynomial fit through the continuum. *Bottom:* The spectrum is normalized using the fit. The spectral line interval is also selected by hand from the spectrum (red part).

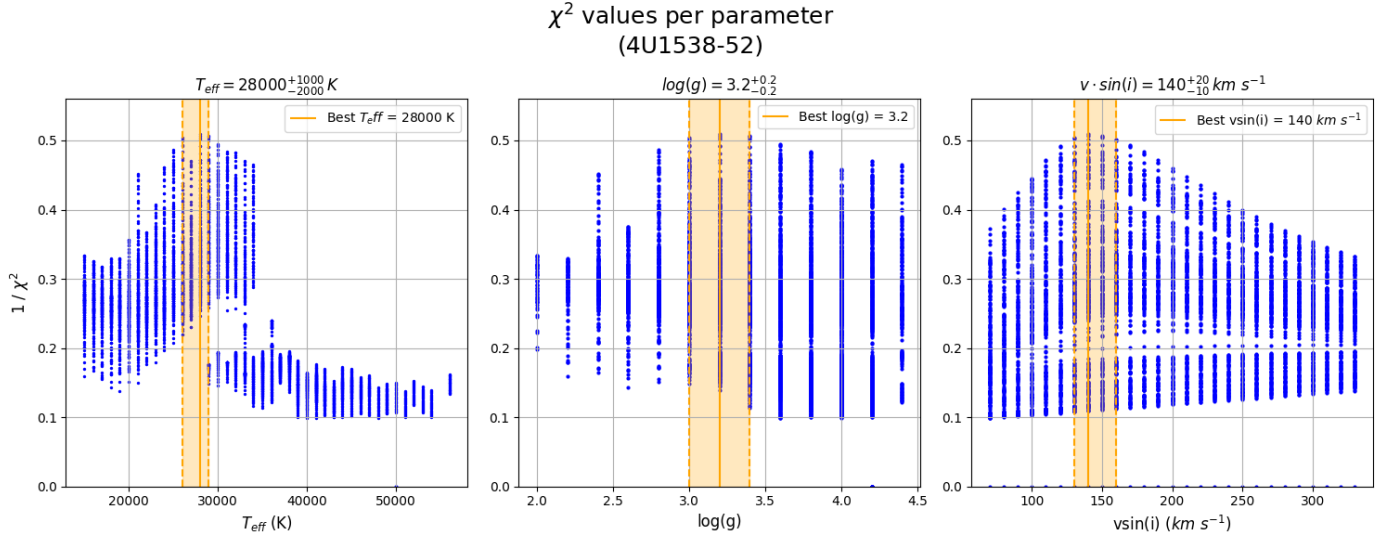


Fig. 7: Result of the model fit for 4U1538-52. The blue dots are all $\frac{1}{\chi^2}$ values. The best fit parameters are represented by the solid orange line and the 95% confidence intervals are represented by the dotted orange lines.

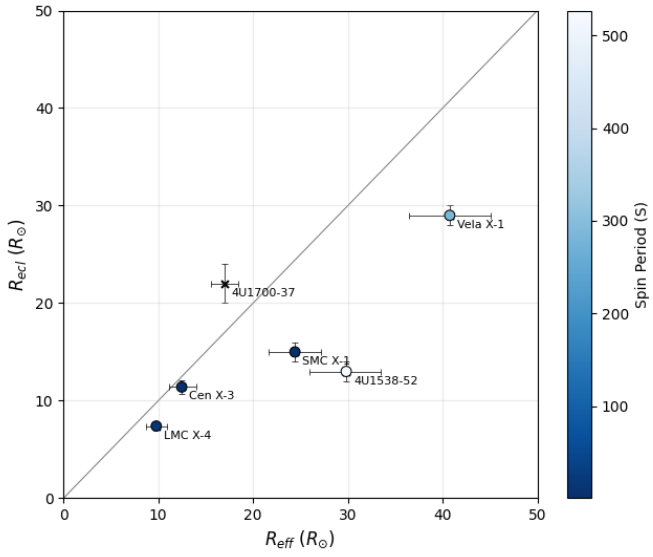


Fig. 8: Comparison of the eclipse radius (R_{ecl}) by Falanga et al. 2015 and the black body radius (R_{eff}). One would expect that these give the same result and that all points are on the vertical line. The color of the data points indicate the spin period of the X-ray pulsars.

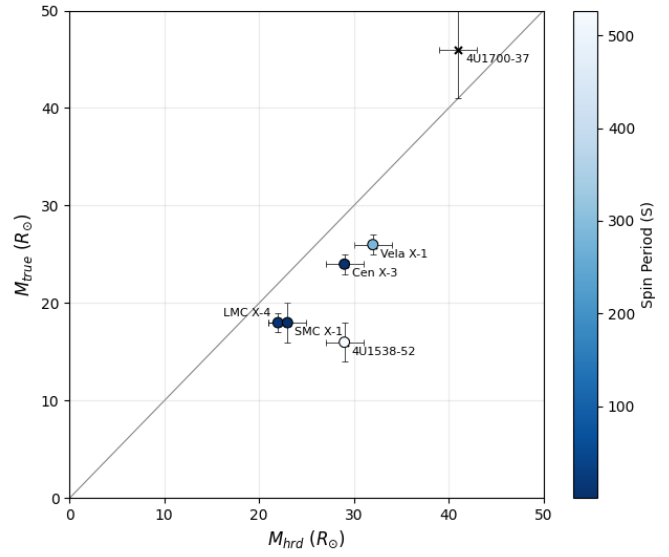


Fig. 10: Comparison of the observed mass (M_{obs}) by Falanga et al. 2015 and the expected mass (M_{hrd}). One would expect the same results and that all points are on the vertical line. The color of the data points indicates the spin period of the X-ray pulsar.

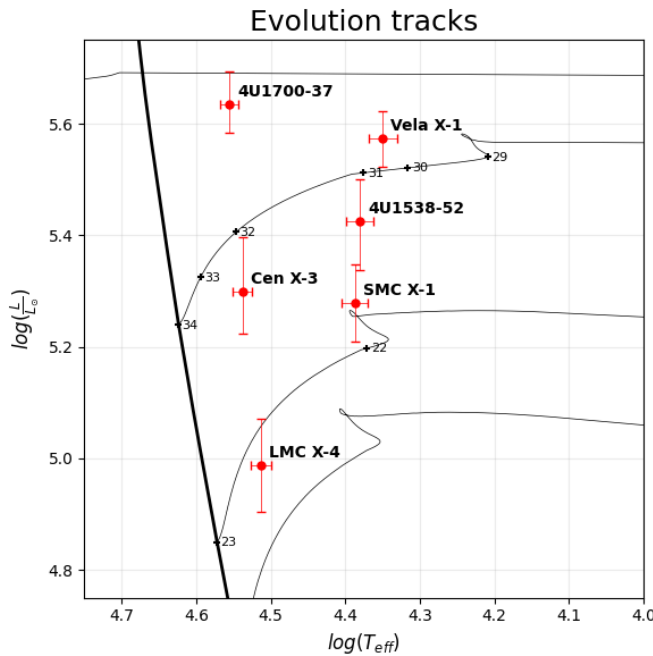


Fig. 9: Hertzsprung Russell Diagram with the luminosity from photometric data (section 3.1) on the vertical axis and the effective temperature based on spectral type (section 3.2.1) on the horizontal axis. The thin black lines are the evolutionary tracks from Chen et al. 2015 for solar metallicity and the thick black line indicates the Zero-Age Main-Sequence. The red dots are the data and the small black crosses indicate the masses for different stages during the evolution.

is important to note that the spectral lines selected for the fitting process are predominantly $He\,I$ lines, with only a few $He\,II$ lines included. The $He\,II$ lines are important since they are more

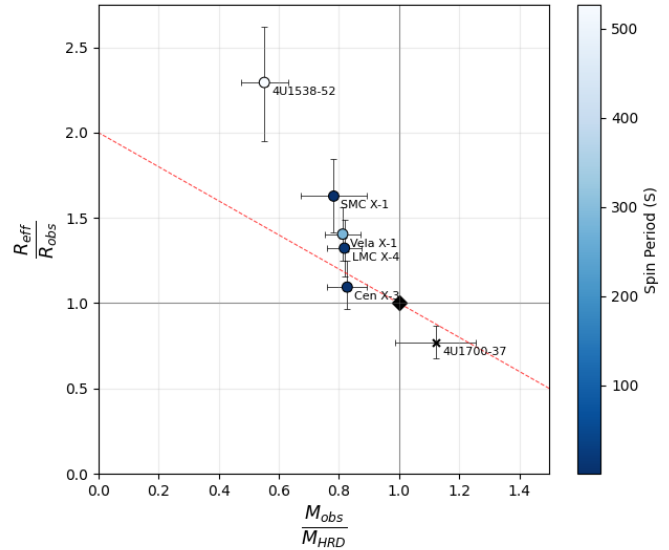


Fig. 11: Fractions of expected and measured masses and radii for five HMXBs. For the optical stars the expected mass (M_{HRD}) and radius (R_{eff}) are derived from the luminosity and effective temperature (section 3.1 & 3.2.1). The eclipse radius (R_{ecl}) is determined from X-ray eclipse measurements and the observed masses (M_{obs}) from X-ray light curves and radial velocity measurements by Falanga et al. 2015. One would expect the masses and radii are equal to each other and that all data points lie on the black diamond on (1, 1). The color of the data points indicate the spin period of the X-ray pulsars.

sensitive to temperature variations, making them important for accurately determining the effective temperature. Unfortunately, only a limited number of $He\,II$ lines were usable in the spectra. Many $He\,II$ lines were either blended with other spectral features or lacked a clear continuum, which made normalizing more difficult. Consequently, the reliance on $He\,I$ lines, which are less

responsive to temperature changes, could have contributed to the discrepancies observed between the model fits and the temperatures based on spectral type of the OB supergiants.

In figure 8, the eclipse radius (R_{ecl}) and black body radius (R_{eff}) are compared, and a similar comparison is made between the expected mass (M_{HRD}) and the observed mass (M_{obs}) in figure 10. One would expect all points to lie on the diagonal line, indicating equal masses and equal radii, as the determination of these parameters should be independent of the method used. However, this is not observed in the data.

For the radius (figure 8), *SMC X-1*, *4U1538-52*, and *Vela X-1* deviate quite significantly from the diagonal line. Note that these three systems all host B-type supergiants. There is no clear explanation for this discrepancy, but it suggests that there may be a systematic issue in determining the effective temperature or luminosity for B-type supergiants. In contrast, the O-type stars, *Cen X-3*, *4U1700-37* and *LMC X-4*, lie much closer to the diagonal line, though they still show slight deviations.

For the mass (figure 10), none of the objects lie on the diagonal line within error bars except for *4U1700-37*. In this case there is no clear distinction between O and B-type stars, suggesting that the earlier observed pattern for the radii might have been coincidental. *4U1538-52* shows the largest relative difference between the two determined masses, which is also the case for the radius.

A different way to plot the data is by comparing the fractions of both masses and radii (figure 11). In this case one would expect all points to be on the black diamond, where the masses and radii are equal. For none of the objects is this the case. All objects lie in the upper left quartile, which indicates that the optical stars are *undersized* and *undermassive* except for *4U1700-37*. This might be due to the fact that *4U1700-37* does not host an X-ray pulsar, making it more difficult to determine the radius and mass with the same accuracy as the other systems.

When comparing figure 11 to figure 2b from Kaper 2001, it is evident that the systems are distributed differently across the diagram. Nevertheless, the optical stars still appear *undermassive* or *undersized*. Notably, in Kaper 2001, *Cen X-3* has the largest offset, whereas in this research, it has the smallest offset. This difference can be explained from the smaller distance used in this study compared to Kaper 2001, resulting in a lower luminosity and smaller offset. In contrast, in this research, *4U1538-52* shows the largest offset. Although its luminosity does not differ significantly from Kaper 2001, the effective temperature derived from the spectral type is 4000K lower in this study, leading to a higher R_{eff} and a larger M_{HRD} and therefore a larger offset in the diagram.

In the figure by Kaper 2001 (figure 2b), a diagonal line is suggested through the data, indicating a possible correlation between the two fractions of masses and radii. This line is also included in figure 11 (red dotted line). While the values differ from Kaper 2001, a similar trend from the bottom right to the upper left is observed. However, this trend cannot be explained by the current data.

One possible explanation for the observed overluminosity is Roche Lobe overflow. In this scenario, the outer envelope of the star is transferred onto the compact object, leading to a decrease in the star's overall mass and radius. However, the core of the star remains unaffected by these changes in the outer layers and retains its luminosity. Making the star too luminous for its mass or vice versa.

For this hypothesis to hold, one would expect the largest offsets in figure 11 for RL overflow systems. These systems are characterized by short pulsar periods, as the pulsar spins-up due

to the transfer of angular momentum. The color of the data points in figure 11 indicate the pulse period of the X-ray pulsars. However, the data does not reveal a clear distinction between RL overflow systems and wind-fed systems, which does not support this hypothesis.

6. Conclusion

This study revisited the physical parameters of OB supergiants in high-mass X-ray binaries (HMXBs) hosting an eclipsing X-ray pulsar to confirm whether these stars are *overluminous*. By using more accurate distance measurements from GaiaDR3 and updated photometric parameters, the luminosity of the OB supergiants was recalculated. New spectral type - T_{eff} relations were used to determine the effective temperature. From these parameters, the black body radius and expected mass were calculated and compared with the eclipse radius from X-ray eclipses and the observed mass derived from X-ray light curves and radial velocity measurements from Falanga et al. 2015.

Although the data in this study is different from Kaper 2001, OB supergiants still appear *overluminous*, and a similar trend is observed for the fractions of radii and masses. However, the exact cause of this phenomenon remains unexplained. The results suggest that Roche lobe overflow is unlikely to account for the observed overluminosity. Further research is needed to investigate the underlying reasons for this discrepancy.

References

- Bailer-Jones, C. A. L., Rybizki, J., Fouesneau, M., Demleitner, M., & Andrae, R. 2021, AJ, 161, 147 [ADS](#)
- Bolton, C. T. & Herbst, W. 1976, AJ, 81, 339 [ADS](#)
- Chaty, S. 2022, Accreting Binaries; Nature, formation, and evolution [ADS](#)
- Chen, Y., Bressan, A., Girardi, L., et al. 2015, MNRAS, 452, 1068 [ADS](#)
- Cherepashchuk, A. M. 1982, Soviet Astronomy Letters, 8, 82 [ADS](#)
- Conti, P. S. 1978, A&A, 63, 225 [ADS](#)
- Crowther, P. A., Lennon, D. J., & Walborn, N. R. 2006, A&A, 446, 279 [ADS](#)
- Falanga, M., Bozzo, E., Lutovinov, A., et al. 2015, A&A, 577, A130 [ADS](#)
- Giacconi, R., Gursky, H., Kellogg, E., Schreier, E., & Tananbaum, H. 1971, ApJ, 167, L67 [ADS](#)
- Graczyk, D., Pietrzyński, G., Thompson, I. B., et al. 2020, ApJ, 904, 13 [ADS](#)
- Hainich, R., Ramachandran, V., Shenar, T., et al. 2019, A&A, 621, A85 [ADS](#)
- Ilovaisky, S. A., Chevalier, C., Motch, C., et al. 1984, A&A, 140, 251 [ADS](#)
- Kaper, L. 2001, in Astrophysics and Space Science Library, Vol. 264, The Influence of Binaries on Stellar Population Studies, ed. D. Vanbeveren, 125 [ADS](#)
- Krzeminski, W. 1974, ApJ, 192, L135 [ADS](#)
- Lejeune, T. & Schaerer, D. 2001, A&A, 366, 538 [ADS](#)
- Liu, Z., Cui, W., Liu, C., et al. 2019, ApJS, 241, 32 [ADS](#)
- Martins, F. & Plez, B. 2006, A&A, 457, 637 [ADS](#)
- Martins, F., Schaerer, D., & Hillier, D. J. 2005, A&A, 436, 1049 [ADS](#)
- Massey, P. 2002, ApJS, 141, 81 [ADS](#)
- Neumann, M., Avakyan, A., Doroshenko, V., & Santangelo, A. 2023, A&A, 677, A134 [ADS](#)
- Pakull, M., van Amerongen, S., Bakker, R., & van Paradijs, J. 1983, A&A, 122, 79 [ADS](#)
- Pietrzyński, G., Graczyk, D., Gallenne, A., et al. 2019, Nature, 567, 200 [ADS](#)
- Schreier, E., Levinson, R., Gursky, H., et al. 1972, ApJ, 172, L79 [ADS](#)
- Subramanian, S. & Subramanian, A. 2009, A&A, 496, 399 [ADS](#)
- Tramper, F., Sana, H., de Koter, A., Kaper, L., & Ramírez-Agudelo, O. H. 2014, A&A, 572, A36 [ADS](#)
- van den Heuvel, E. P. J. 1976, in IAU Symposium, Vol. 73, Structure and Evolution of Close Binary Systems, ed. P. Eggleton, S. Mitton, & J. Whelan, 35 [ADS](#)
- van den Heuvel, E. P. J. & Heise, J. 1972, Nature Physical Science, 239, 67 [ADS](#)
- Wang, S. & Chen, X. 2019, ApJ, 877, 116 [ADS](#)
- Wang, S. & Chen, X. 2023, ApJ, 946, 43 [ADS](#)
- Zorec, J., Cidale, L., Arias, M. L., et al. 2009, A&A, 501, 297 [ADS](#)

Appendix A: Stellar Models

Table A.1: Photometric and stellar parameters from the models from [Martins & Plez 2006](#) and [Martins et al. 2005](#).

ST	T_{eff} [K]	$^{10} \log \left(\frac{L}{L_\odot} \right)$	$R_{spec}[R_\odot]$	$M_{spec}[M_\odot]$	M_v	M_h	$(B - V)_0$	$(J - H)_0$	BC_v	BC_h
O3V	44852	5.840	13.800	57.950	-5.860	-5.070	-0.280	-0.110	-3.990	-4.780
O4V	42857	5.670	12.420	46.940	-5.570	-4.790	-0.280	-0.110	-3.850	-4.630
O5V	40862	5.490	11.200	38.080	-5.270	-4.490	-0.280	-0.110	-3.710	-4.480
O5.5V	39865	5.410	10.640	34.390	-5.140	-4.370	-0.280	-0.110	-3.640	-4.400
O6V	38867	5.320	10.110	30.980	-4.990	-4.220	-0.280	-0.110	-3.560	-4.330
O6.5V	37870	5.230	9.610	28.000	-4.840	-4.080	-0.270	-0.110	-3.480	-4.240
O7V	36872	5.140	9.150	25.290	-4.700	-3.940	-0.270	-0.110	-3.400	-4.160
O7.5V	35874	5.050	8.700	22.900	-4.560	-3.800	-0.270	-0.110	-3.320	-4.070
O8V	34877	4.960	8.290	20.760	-4.410	-3.670	-0.270	-0.110	-3.240	-3.980
O8.5V	33879	4.860	7.900	18.800	-4.250	-3.510	-0.270	-0.110	-3.150	-3.890
O9V	32882	4.770	7.530	17.080	-4.120	-3.380	-0.270	-0.110	-3.060	-3.800
O9.5V	31884	4.680	7.180	15.550	-3.980	-3.250	-0.260	-0.110	-2.970	-3.700
O3III	44537	5.960	16.190	55.950	-6.180	-5.400	-0.280	-0.110	-3.970	-4.750
O4III	42422	5.850	15.610	47.430	-6.050	-5.270	-0.280	-0.110	-3.820	-4.600
O5III	40307	5.730	15.070	40.430	-5.910	-5.140	-0.280	-0.110	-3.670	-4.440
O5.5III	39249	5.670	14.820	37.350	-5.840	-5.070	-0.280	-0.110	-3.590	-4.360
O6III	38192	5.610	14.580	34.530	-5.770	-5.000	-0.270	-0.110	-3.510	-4.270
O6.5III	37134	5.540	14.360	31.960	-5.680	-4.920	-0.270	-0.110	-3.420	-4.180
O7III	36077	5.480	14.140	29.590	-5.610	-4.860	-0.270	-0.110	-3.340	-4.090
O7.5III	35019	5.420	13.930	27.450	-5.550	-4.800	-0.270	-0.110	-3.250	-4.000
O8III	33961	5.350	13.740	25.490	-5.470	-4.720	-0.270	-0.110	-3.160	-3.900
O8.5III	32904	5.280	13.550	23.680	-5.390	-4.650	-0.270	-0.110	-3.060	-3.800
O9III	31846	5.210	13.380	22.040	-5.310	-4.580	-0.260	-0.110	-2.960	-3.700
O9.5III	30789	5.150	13.220	20.550	-5.260	-4.530	-0.260	-0.110	-2.860	-3.590
O3I	42233	5.990	18.560	67.530	-6.420	-5.640	-0.280	-0.110	-3.810	-4.590
O4I	40422	5.930	18.990	58.540	-6.400	-5.630	-0.280	-0.110	-3.680	-4.450
O5I	38612	5.870	19.450	50.720	-6.390	-5.620	-0.280	-0.110	-3.540	-4.300
O5.5I	37706	5.840	19.700	47.250	-6.380	-5.620	-0.270	-0.110	-3.470	-4.230
O6I	36801	5.810	19.950	44.100	-6.380	-5.620	-0.270	-0.110	-3.400	-4.150
O6.5I	35895	5.780	20.220	41.200	-6.380	-5.620	-0.270	-0.110	-3.320	-4.080
O7I	34990	5.750	20.490	38.440	-6.380	-5.630	-0.270	-0.110	-3.240	-4.000
O7.5I	34084	5.720	20.790	36.000	-6.380	-5.640	-0.270	-0.110	-3.170	-3.910
O8I	33179	5.680	21.100	33.720	-6.360	-5.620	-0.270	-0.110	-3.090	-3.830
O8.5I	32274	5.650	21.410	31.540	-6.370	-5.630	-0.260	-0.110	-3.000	-3.740
O9I	31368	5.610	21.760	29.630	-6.360	-5.620	-0.260	-0.110	-2.920	-3.650
O9.5I	30463	5.570	22.110	27.830	-6.340	-5.620	-0.260	-0.110	-2.830	-3.560

Appendix B: Radial velocity Cen X-3

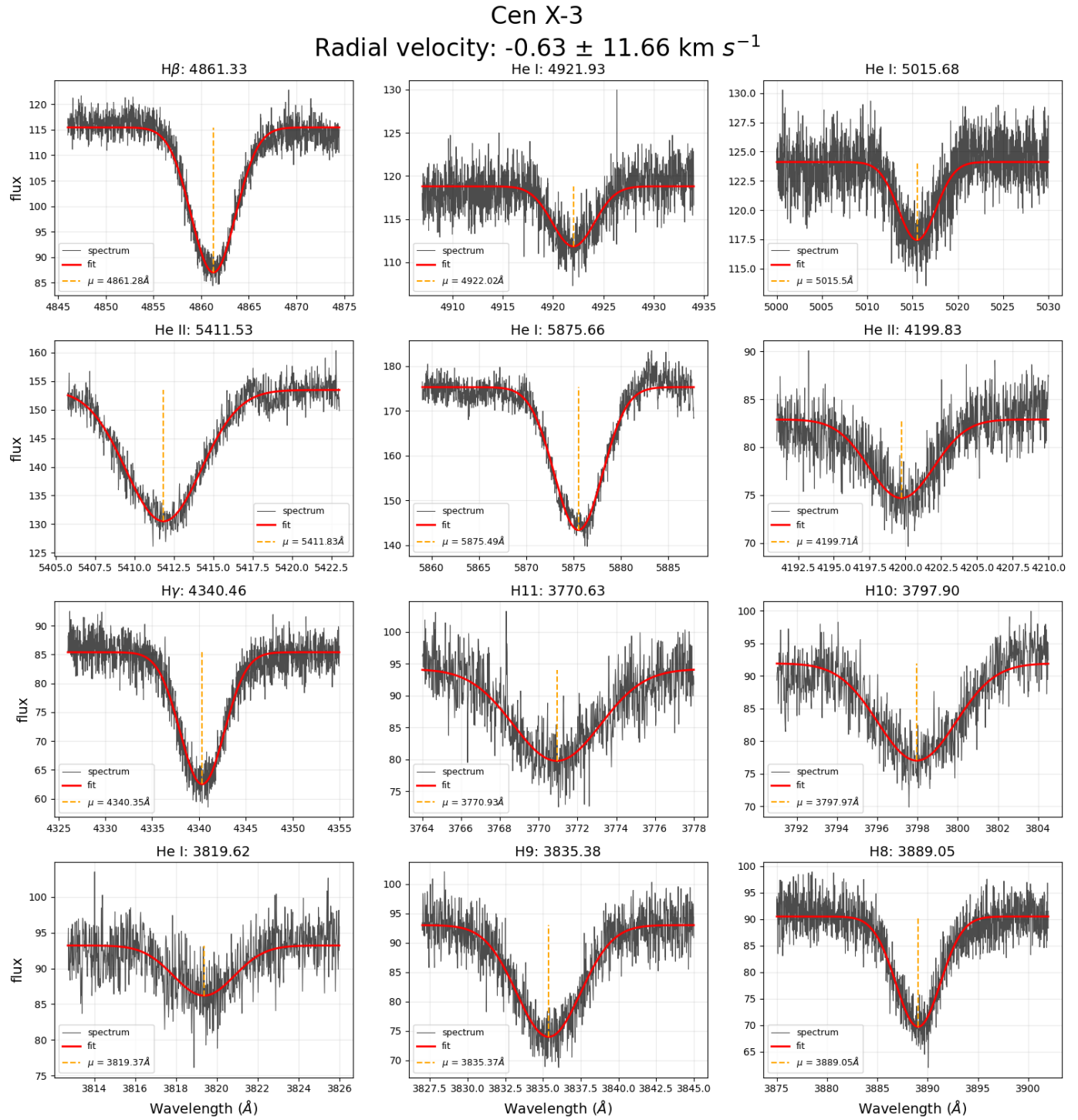
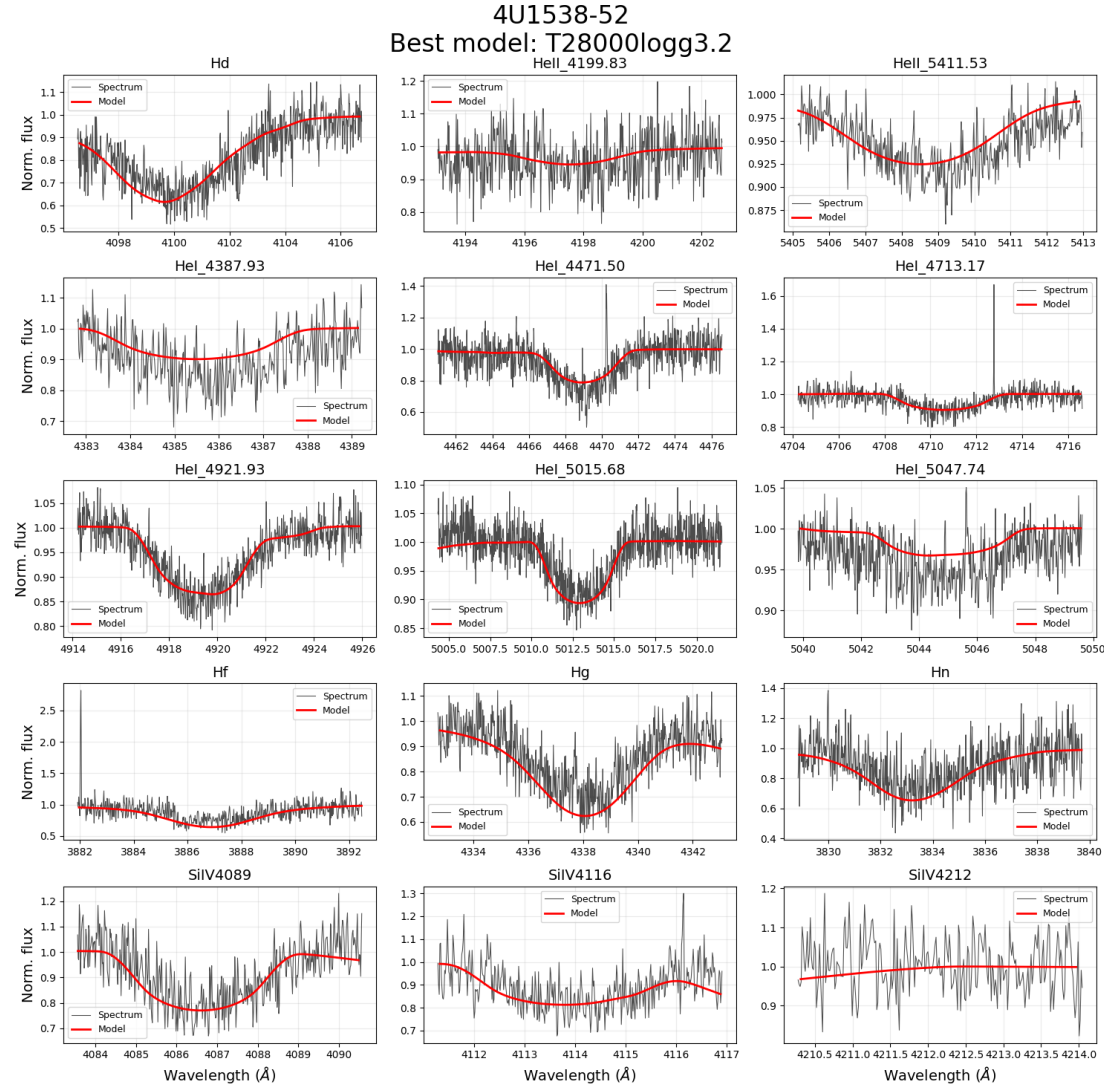


Fig. B.1: The radial velocity determination for Cen X-3. The red lines are Gaussian fits to a selection of spectral lines to determine their Doppler shifts. The overall radial velocity is the average of the Doppler shifts. The error is the standard deviation on the radial velocities.

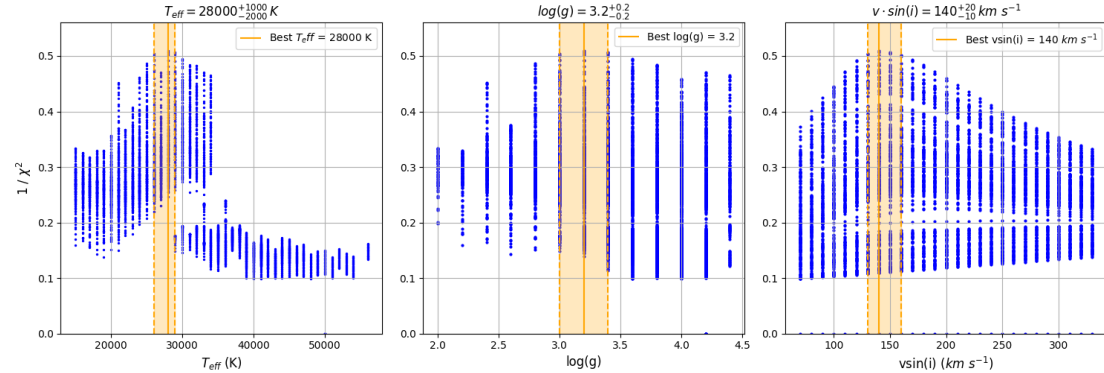
Appendix C: Model fit results

Appendix C.1: 4U1538-52



(a) The best fitting model plotted over the spectral lines.

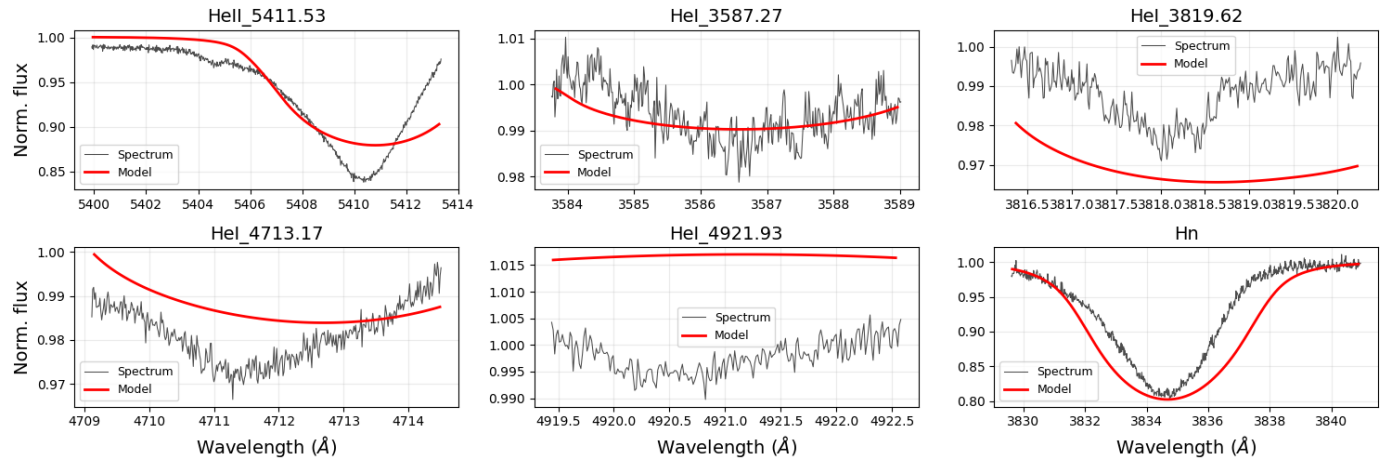
χ^2 values per parameter
(4U1538-52)



(b) Result of the model fit. The blue dots are all $\frac{1}{\chi^2}$ values. The best fit parameters are represented by the solid orange line and the 95% confidence intervals are represented by the dotted orange lines.

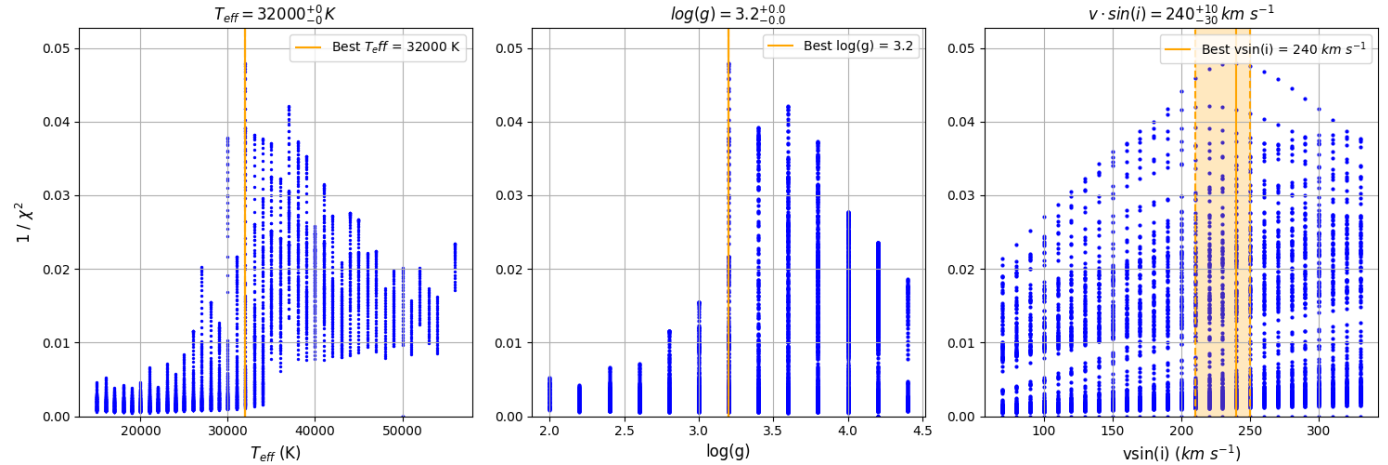
Fig. C.1: Best fit for 4U1538-52.

4U1700-37
Best model: T32000logg3.2



(a) The best fitting model plotted over the spectral lines.

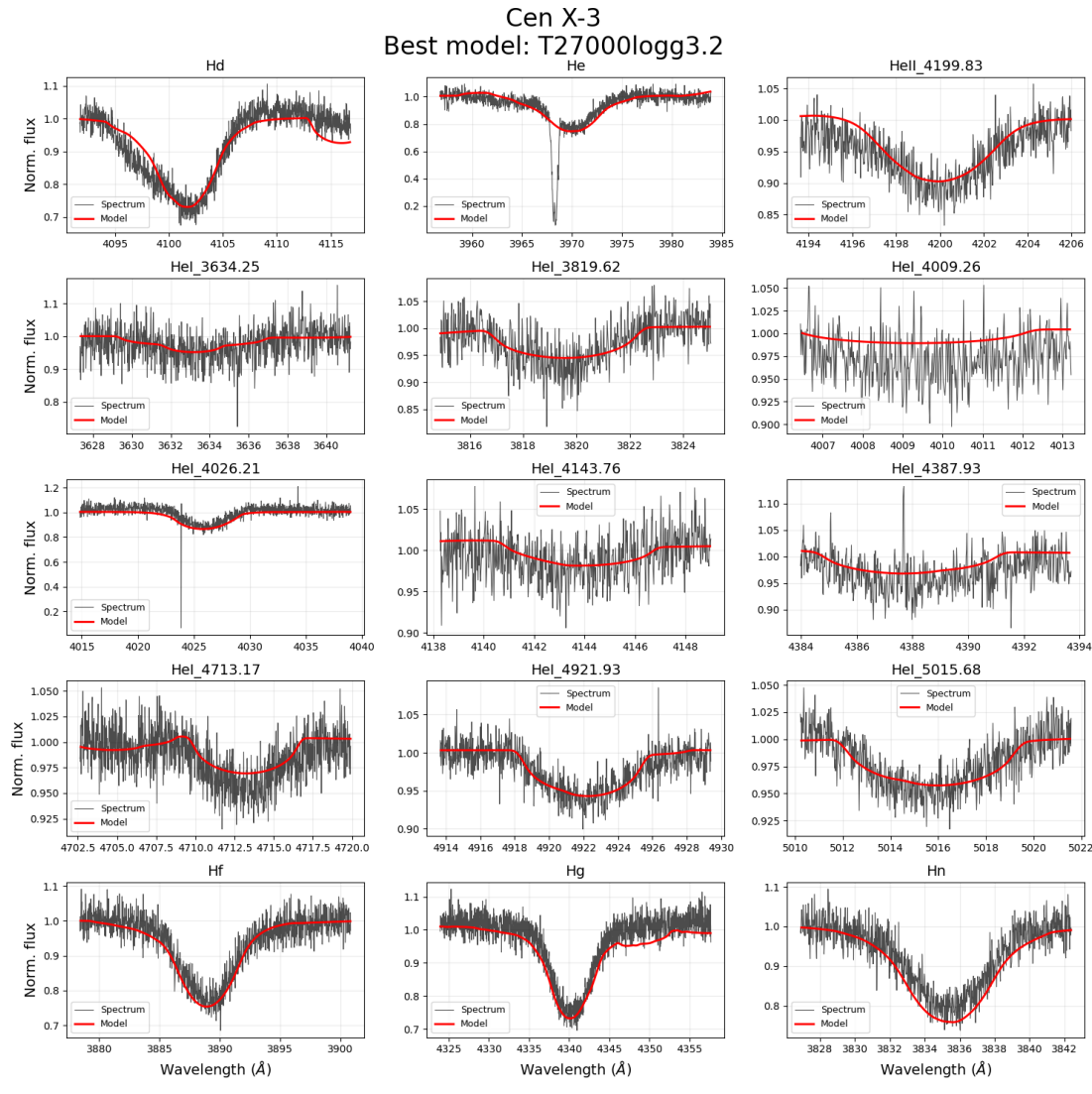
χ^2 values per parameter
(4U1700-37)



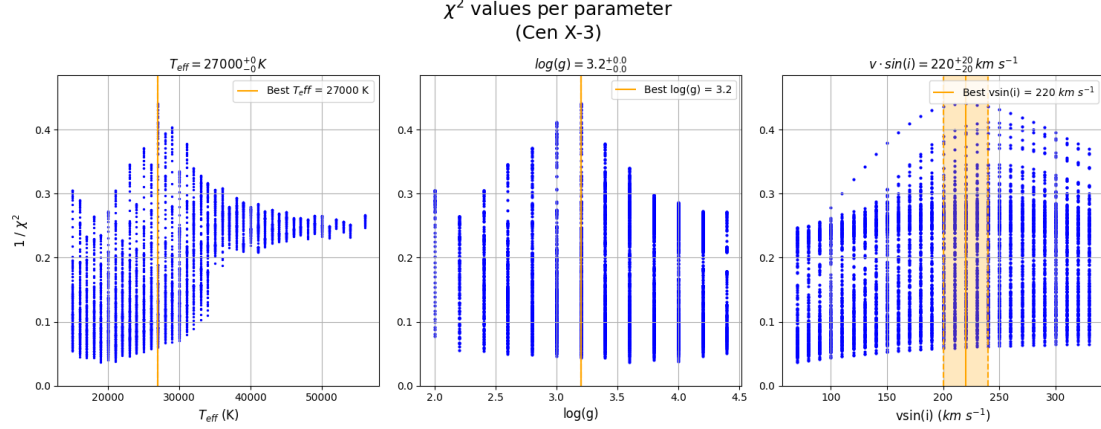
(b) Result of the model fit. The blue dots are all $\frac{1}{\chi^2}$ values. The best fit parameters are represented by the solid orange line and the 95% confidence intervals are represented by the dotted orange lines.

Fig. C.2: Best fit for 4U1700-37.

Appendix C.3: Cen X-3



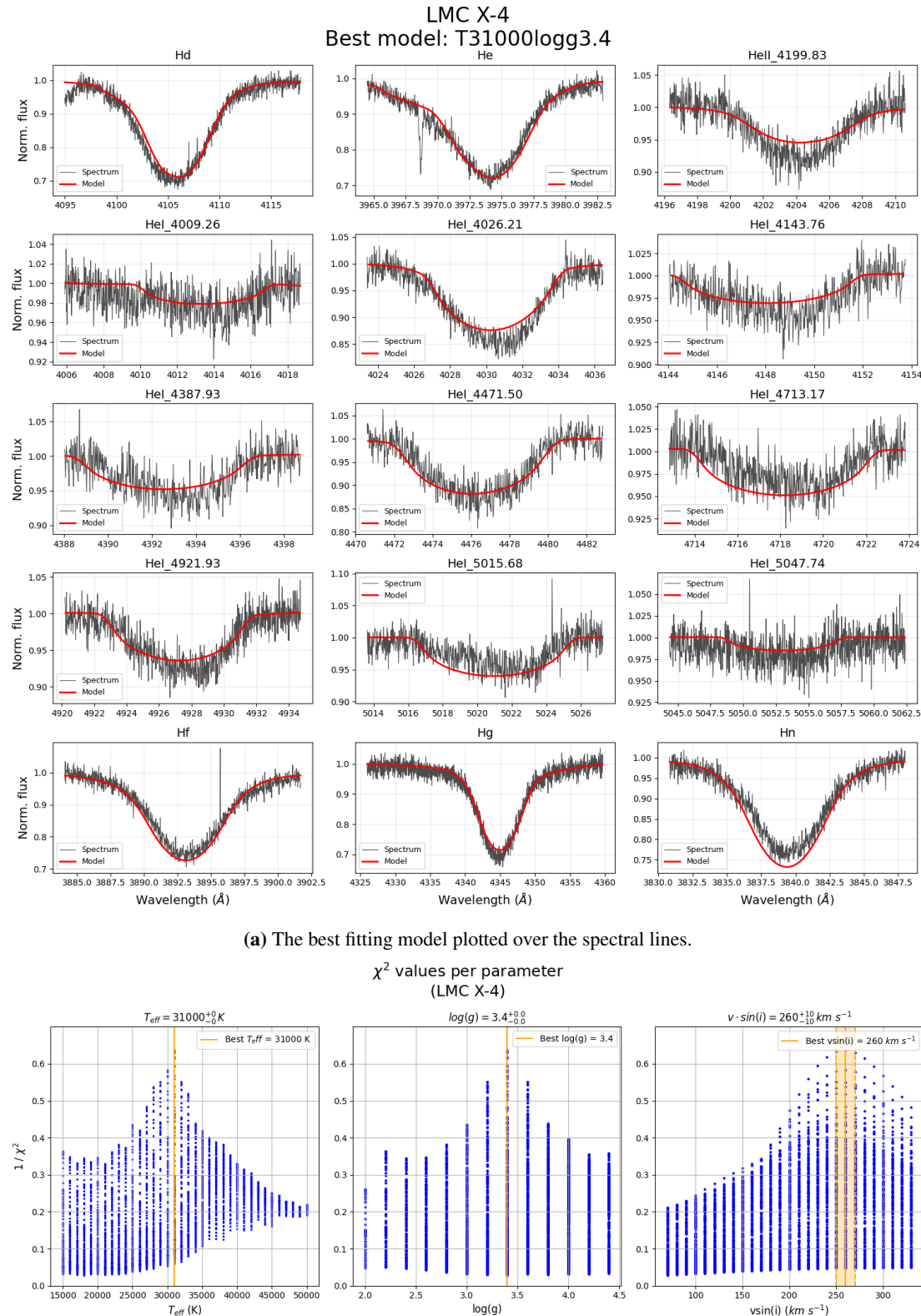
(a) The best fitting model plotted over the spectral lines.



(b) Result of the model fit. The blue dots are all $\frac{1}{\chi^2}$ values. The best fit parameters are represented by the solid orange line and the 95% confidence intervals are represented by the dotted orange lines.

Fig. C.3: Best fit for *Cen X-3*.

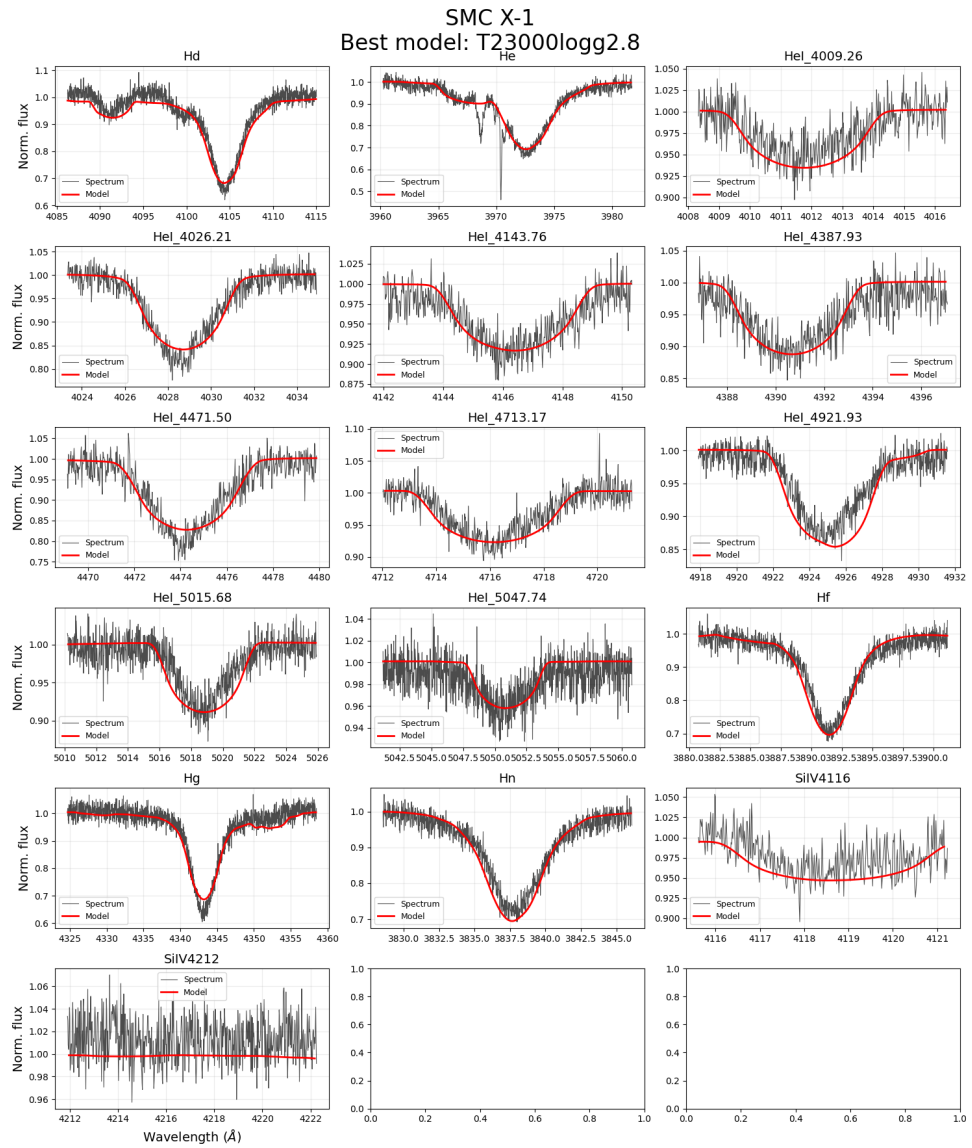
Appendix C.4: LMC X-4



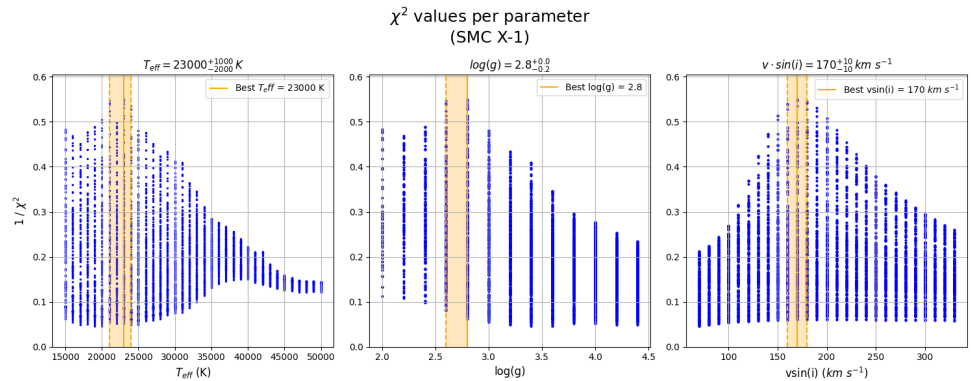
(b) Result of the model fit. The blue dots are all $\frac{1}{\chi^2}$ values. The best fit parameters are represented by the solid orange line and the 95% confidence intervals are represented by the dotted orange lines.

Fig. C.4: Best fit for LMC X-4.

Appendix C.5: SMC X-1



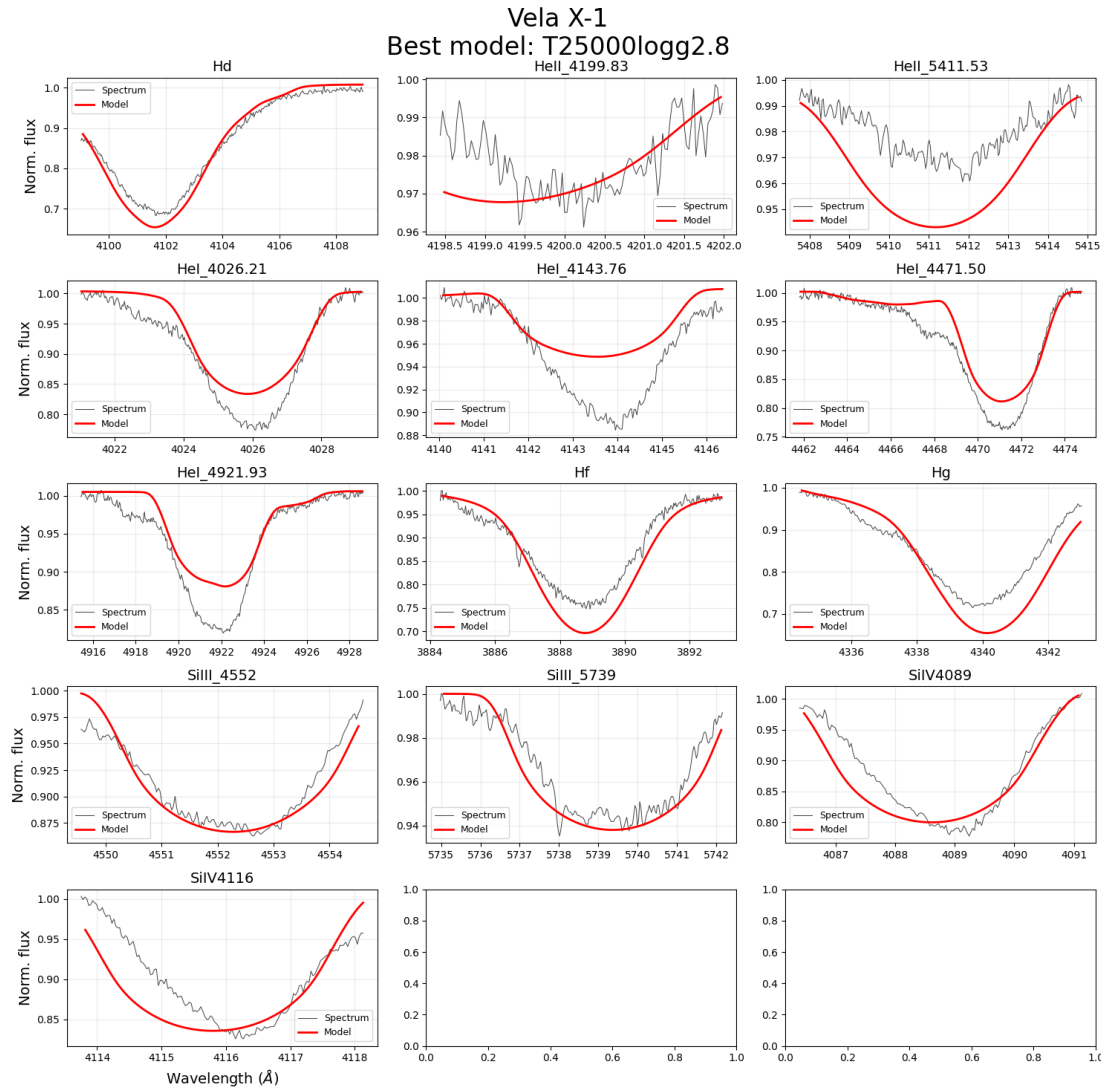
(a) The best fitting model plotted over the spectral lines.



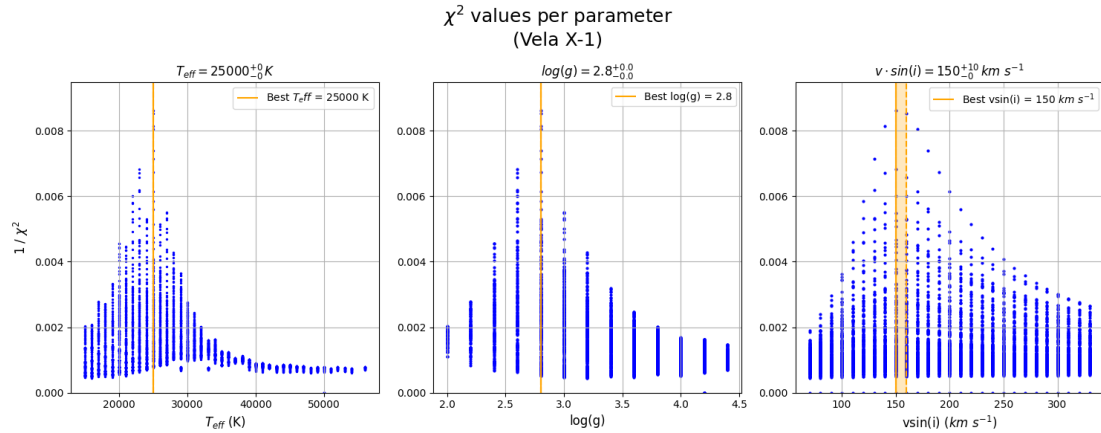
(b) Result of the model fit. The blue dots are all $\frac{1}{\chi^2}$ values. The best fit parameters are represented by the solid orange line and the 95% confidence intervals are represented by the dotted orange lines.

Fig. C.5: Best fit for SMC X-1.

Appendix C.6: Vela X-1



(a) The best fitting model plotted over the spectral lines.



(b) Result of the model fit. The blue dots are all $\frac{1}{\chi^2}$ values. The best fit parameters are represented by the solid orange line and the 95% confidence intervals are represented by the dotted orange lines.

Fig. C.6: Best fit for LMC X-4.